

IMPROVING THE MODEL OF EMISSION FROM SPINNING DUST: EFFECTS OF GRAIN WOBBLING AND TRANSIENT SPIN-UP

THIEM HOANG¹, B. T. DRAINE² AND A. LAZARIAN¹

Draft version March 11, 2022

ABSTRACT

Observations continue to support the interpretation of the anomalous microwave foreground as electric dipole radiation from spinning dust grains as proposed by Draine & Lazarian (1998ab). In this paper we present a refinement of the original model by improving the treatment of a number of physical effects. First, we consider a *disk-like* grain rotating with angular velocity at an arbitrary angle with respect to the grain symmetry axis (i.e., grain wobbling) and derive the rotational damping and excitation coefficients arising from infrared emission, plasma-grain interactions and electric dipole emission. The angular velocity distribution function and the electric dipole emission spectrum for disk-like grains are calculated using the Langevin equation, for cases both with and without fast internal relaxation. Our results show that for fast internal relaxation, the peak emissivity of spinning dust, compared to earlier studies, increases by a factor of ~ 2 for the Warm Neutral Medium (WNM), the Warm Ionized Medium (WIM), the Cold Neutral Medium (CNM) and the Photodissociation Region (PDR), and by a factor ~ 4 for Reflection Nebulae (RN). The frequency at the emission peak also increases by factors ~ 1.4 to ~ 2 for these media. Without internal relaxation, the increase of emissivity is comparable, but the emission spectrum is more extended to higher frequency. The increased emission results from the non-sphericity of grain shape and from the anisotropy in damping and excitation along directions parallel and perpendicular to the grain symmetry axis. Second, we provide a detailed numerical study including transient spin-up of grains by single-ion collisions. The range of grain size in which single-ion collisions are important is identified. The impulses broaden the emission spectrum and increase the peak emissivity for the CNM, WNM and WIM, although the increases are not as large as those due to the grain wobbling. In addition, we present an improved treatment of rotational excitation and damping by infrared emission.

Subject headings: ISM: dust, extinction — ISM: general — galaxies: ISM — infrared: galaxies

1. INTRODUCTION

Diffuse Galactic microwave emission in the 10 – 100 GHz frequency range carries important information on the fundamental properties of the interstellar medium, but it also interferes with Cosmic Microwave Background (CMB) experiments (see Bouchet et al. 1999, Tegmark et al. 2000, Efstathiou 2003).

It used to be thought that there were only three major components of the diffuse microwave Galactic foreground: synchrotron emission, free-free radiation from plasma (thermal bremsstrahlung) and thermal emission from dust. However, in the range of frequency from 10 to 100 GHz an anomalous microwave foreground which was difficult to reconcile with the components above was first reported by Kogut et al. (1996a, 1996b).

de Oliveira-Costa et al. (2002) gave this emission the nickname “Foreground X”, reflecting its mysterious nature. This component is spatially correlated with 100 μm thermal emission from dust, but its intensity is much higher than one would expect by extrapolating the thermal dust emission spectrum to the microwave range. Draine & Lazarian (1998a,b) proposed that this foreground was electric dipole radiation from ultrasmall spinning dust grains. Although such emission from spinning dust had been discussed previously (see Erickson 1957,

Ferrara & Dettmar 1994), DL98a were the first to include the variety of excitation and damping processes that are relevant for very small grains. As time went on alternative models for the enigmatic foreground have appeared to be inconsistent with observations³, while the predictions of the spinning dust model have thus far been confirmed. As a result, spinning dust is now the principal explanation for the mysterious “Foreground X”.

Although the model in Draine & Lazarian (1998ab) provided quantitative predictions consistent with observational data, the current state of precision measurement of the foregrounds calls for refinement of the model, using a better description of the complex grain dynamics and modifying some of the original assumptions.

Recent studies showed that the correspondence of the DL98 model to observations can be improved by adjusting the parameters of the model. For instance, Dobler et al. (2009) used the Wilkinson Microwave Anisotropy Probe (WMAP) 5 year data to show that a broad bump with frequency at $\sim 40\text{GHz}$ correlated with $\text{H}\alpha$, a tracer of the warm ionized medium (WIM). They showed that this bump is consistent with predictions from a DL98 model modified so that grains have a characteristic dipole moment of 3.5 D at grain size 1 nm, and the gas number density of the WIM is $n_{\text{H}} = 0.15\text{ cm}^{-3}$ (cf. $n_{\text{H}} =$

¹ Astronomy Department, University of Wisconsin, Madison, WI 53706

² Department of Astrophysical Sciences, Princeton University, Princeton, NJ 08544

³ For instance, the dust-correlated synchrotron emission suggested by Bennett et al. (2003) has now been ruled out (see de Oliveira-Costa et al. 1999, Finkbeiner, Langston, & Minter 2004, Boughn & Pober 2007, Gold et al. 2009, 2010).

0.1 cm^{-3} in the DL98 model).

On the theoretical front, Ali-Haïmoud et al. (2009) improved the accuracy of predictions of the model of emission from spinning dust using the Fokker-Planck equation for the angular velocity ω . The authors quantified the deviations of the grain angular velocity distribution function from the Maxwellian approximation that had been used by DL98b for the sake of simplicity. With the other assumptions being identical to DL98b, their findings are not much different from DL98b's predictions. However, both the DL98 model and the refined model by Ali-Haïmoud et al. (2009) disregarded the non-sphericity of grains and the anisotropy in the damping and excitation processes. Obviously, this assumption is inexact for non-spherical grains or when there exists any anisotropy in the damping and excitation processes. This present paper is intended to go deeper into studies of grain dynamics for a disk-like grain geometry, relaxing more of the simplifying assumptions in the original DL98b treatment.

The main thrust of our present work is to provide a better description of several physical processes which have not been addressed in their complexity either in DL98b or the papers that followed. In particular: (i) the effects on electric dipole emission arising from the wobbling of the axis of major inertia of the *disk-like* grain around the angular momentum due to internal relaxation and the anisotropy of grain rotational damping and excitation (not yet been treated in the literature, so far as we are aware); and (ii) transient spin-up of very small grains due to single-ion collisions.

First of all, the former process, i.e., imperfect internal alignment in the non-spherical grain, can alter the frequency at which the electric dipole emits. In the DL98 model, the emission frequency is identical to the angular frequency $\omega/2\pi$. However, if the dipole moment is fixed in the grain body, then the complex motion of the grain axes around the angular momentum \mathbf{J} will result in emission at frequencies different from its angular frequency.

In addition, imperfect alignment is essential for many astrophysical processes, e.g., for grain alignment (see Lazarian 2007 and Lazarian & Hoang 2009 for recent reviews). In our quest to understand the rotational dynamics of grains which do not rotate about their axis of major inertia we capitalize on improved understanding of internal randomization arising from thermal fluctuations within the grain (Lazarian 1994, Lazarian & Roberge 1997, Weingartner 2009, Hoang & Lazarian 2009). Disalignment of the grain's principal axis from the direction of the angular momentum \mathbf{J} will cause the angular velocity to increase, leading to increased electric dipole emission at high frequency. Our paper provides a quantitative description of the effect on the spinning dust emissivity.

The latter process – collisions with ions – is important for small grains where the angular momentum of an impinging ion can be larger than the pre-collision grain angular momentum, resulting in a rotational excitation spike. In DL98b it was noted that the effect is expected to increase the spinning dust emissivity, but no quantitative description was given.

While the treatment of high impulse ion collisions is easily performed within our Langevin code, the treatment of grain wobbling for non-spherical grains requires a careful and somewhat tedious modification of our treat-

ment of the angular momentum diffusion and damping in the DL98 model. In particular, we have to consider separately parallel and perpendicular contributions to grain damping and excitation. In addition, we provide an improved treatment of infrared emission from spinning dust grains.

The structure of the paper is as follows. In §2, we present elements of the DL98 model and our modifications to that model. In §3 we provide detailed calculations for rotational damping and excitations arising from plasma-grain interactions and electric dipole emission for the disk-like grain geometry. Refined calculations for the effects of infrared emission are presented in §4 and 5. In §6, we study the effect of the grain precession on the electric dipole emission spectrum and identify its frequency modes. In §7 and 8 we present our numerical techniques for finding the distribution functions of grain angular velocity and electric dipole emission, and benchmark calculations. In §9, we present our results for emissivities from spinning dust for various idealized environments, and clarify the role of grain shape and differential rotational damping and excitation processes to the increase of peak emissivity and frequency. Discussion and summary are presented in §10 and 11, respectively.

2. REVISITING THE DL98 MODEL

2.1. Elements of the DL98 model

Here we present the grain model and our notation. DL98 pointed out that the abundant polycyclic aromatic hydrocarbon (PAH) particles required to explain the observed infrared emission provide a population of particles that must be spinning and emitting electric dipole radiation in rotational transitions. The smaller PAH particles are expected to be planar. The grain size a is defined as the radius of a sphere of equivalent volume. Grains are assumed to be disk-like with height L and radius R for $a < a_2$ and spherical for $a \geq a_2$. $a_2 = 6 \times 10^{-8}$ cm is chosen in DL98b. The surface equivalent radius a_s is defined to be the radius of the sphere with the same surface area of the grain. The excitation equivalent radius a_x is defined to be the radius of the sphere with the same $\int r^2 dS$ with r being the distance from the surface element dS to the center of mass of the grain (see Appendix A).

The electric dipole moment μ of a grain arises from the intrinsic electric dipole moment associated with asymmetric molecules or substructures, and from the asymmetric distribution of any excess charge present. The latter is shown to be less important.

A grain acquires charge through collisions with ions and electrons in gas, and through photoemission. Assuming that the charging and photoemission are in equilibrium (i.e., ionization equilibrium), the distribution of grain charge $f(Z)$ for a given grain size can be obtained by solving the ionization equilibrium equations (see Draine & Sutin 1987, Weingartner & Draine 2001b).

A grain in the gas experiences collisions with atoms and ions, plasma-grain interactions, infrared emission and electric dipole emission. All these processes result in damping and excitation of grain rotation. DL98b assumed that the angular velocity ω is perfectly aligned with the grain axis of major inertia \mathbf{a}_1 , and isotropically oriented in space, and derived the damping and exci-

tation coefficients assuming perfect internal alignment. The dimensionless damping and excitation coefficients, F and G are defined as

$$F_j = -\frac{\tau_H}{\omega_j} \frac{d\omega_j}{dt}, \quad (1)$$

$$G_j = \frac{\tau_H}{2k_B T_{\text{gas}}} \frac{I_{\parallel} d\omega_j^2}{dt}, \quad (2)$$

where $j=n, i, p$ and IR denote collisions of the grain with neutral, ion, plasma-grain interactions and infrared emission, $(1/2)I_{\parallel}d\omega_j^2/dt$ is the increase of kinetic energy of rotation along one axis due to the excitation process j ; τ_H is the damping time of the grain in a purely H I gas of temperature T_{gas} , and I_{\parallel} is the moment of inertia along the grain symmetry axis. For an uncharged grain in a gas of purely atomic hydrogen, $F_H = G_H = 1$.

The emissivity per H due to the electric dipole emission of spinning dust with angular velocity ω is

$$\frac{j_{\nu}}{n_H} = \frac{1}{4\pi} \frac{1}{n_H} \int_{a_{\min}}^{a_{\max}} da \frac{dn}{da} 4\pi\omega^2 f_{\omega} 2\pi \left(\frac{2\mu_{\perp}^2 \omega^4}{3c^3} \right), \quad (3)$$

where n_H is the density of H nuclei, f_{ω} is the distribution function for the angular velocity ω , μ_{\perp} is the electric dipole moment perpendicular to the rotation axis, and dn/da is the grain size distribution function with a in the range from a_{\min} to a_{\max} . Here we take the grain size distribution from Draine & Li (2007), and consider only carbonaceous grains. In the DL98 model, for the sake of simplicity, f_{ω} was assumed to be a Maxwellian distribution.

2.2. Our improvements of the DL98 model

Both the DL98 model and the refined model by Al-Haïmoud et al. (2009) assumed that very small grains have disk-like shape and large grains are spherical, but they ignored the non-sphericity of grain shape when calculating the rotational distribution function and emissivity. In the present paper, we modify the DL98 model as follows.

First, we consider the rotation of a disk-like grain with angular velocity ω not perfectly aligned with its symmetry axis (i.e. grain wobbling or imperfect alignment), relaxing the assumption of the perfect internal alignment of ω with the symmetry axis in the DL98 model. The rotational damping and excitation coefficients parallel and perpendicular to the grain symmetry axis resulting from grain infrared emission, plasma-grain interactions and electric dipole emission are then derived.

Second, we will identify the frequency modes of dipole emission as a result of complex motion of the grain axes with respect to a fixed angular momentum \mathbf{J} .

Third, we will find the exact distribution functions for angular velocity f_{ω} and electric dipole emission frequency f_{ν} for *non-spherical* grains using numerical simulations of the Langevin equation (LE), instead of assuming the Maxwellian distribution as in the DL98 model or using the Fokker-Planck equation (FP) as in Ali-Haïmoud et al. (2009). Using the LE approach, we investigate the effect of grain wobbling on the emission spectrum of spinning dust. The effect of internal thermal fluctuations, which results in deviation of the grain symmetry axis

from the angular momentum \mathbf{J} (Lazarian 1994; Lazarian & Roberge 1997), is also studied.

Finally, the transient rotational spin-up due to single-ion collisions with very small grains is numerically studied using the LE, in which single-ion collisions are treated as Poisson-distributed discrete events.

To see how the grain wobbling can modify results from the DL98 model, let us consider the simple case of 3D rotation for an axisymmetric grain with principal moments of inertia $I_1 > I_2 = I_3$ along principal axes \mathbf{a}_1 , \mathbf{a}_2 and \mathbf{a}_3 , respectively. Denote $I_{\parallel} = I_1$ and $I_{\perp} = I_2 = I_3$. The ratio of moments of inertia is defined as $h = I_{\parallel}/I_{\perp}$.⁴ For the moment, we ignore the damping due to the electric dipole emission. Assuming that the rotation along three principal axes are independent, the mean square angular velocity for this case is

$$\langle \omega^2 \rangle = \langle \omega_{\parallel}^2 \rangle + 2\langle \omega_{\perp}^2 \rangle, \quad (4)$$

where $\langle \omega_{\perp}^2 \rangle = \langle \omega_2^2 \rangle = \langle \omega_3^2 \rangle$. The mean square angular velocities along the parallel and perpendicular direction to the symmetry axis are given by (see DL98b)

$$\langle \omega_{\parallel, \perp}^2 \rangle = \frac{G_{\parallel, \perp}}{F_{\parallel, \perp}} \frac{k_B T_{\text{gas}}}{I_{\parallel, \perp}}, \quad (5)$$

where $F_{\parallel, \perp}$ and $G_{\parallel, \perp}$ are total damping and excitation coefficients defined by equations (1) and (2) corresponding to the rotation parallel and perpendicular to the grain symmetry axis. After some manipulations, we get

$$\langle \omega^2 \rangle = 3\langle \omega_{\parallel}^2 \rangle + \frac{G_{\parallel}}{F_{\parallel}} \frac{2k_B T_{\text{gas}}}{I_{\parallel}} \left(\frac{\alpha_{\parallel}}{\alpha_{\perp}} - 1 \right), \quad (6)$$

where

$$\alpha_{\parallel} = \frac{I_{\parallel} F_{\parallel}}{G_{\parallel}}, \quad \alpha_{\perp} = \frac{I_{\perp} F_{\perp}}{G_{\perp}}. \quad (7)$$

Therefore, the increase of mean square angular velocity becomes

$$\frac{\langle \omega^2 \rangle - 3\langle \omega_{\parallel}^2 \rangle}{3\langle \omega_{\parallel}^2 \rangle} \equiv \frac{\langle \omega^2 \rangle - \langle \omega^2 \rangle_{\text{DL98}}}{\langle \omega^2 \rangle_{\text{DL98}}} = \frac{2}{3} \left(\frac{\alpha_{\parallel}}{\alpha_{\perp}} - 1 \right), \quad (8)$$

where $\langle \omega^2 \rangle_{\text{DL98}} = 3\langle \omega_{\parallel}^2 \rangle = (G_{\parallel}/F_{\parallel}) \times (3k_B T_{\text{gas}}/I_{\parallel})$.

It can be seen that the excess of mean square angular velocity of the grain depends only on the ‘‘anisotropy ratio’’

$$\eta = \frac{\alpha_{\parallel}}{\alpha_{\perp}} = h \times \left(\frac{F_{\parallel} G_{\perp}}{F_{\perp} G_{\parallel}} \right). \quad (9)$$

The anisotropy can arise from the non-sphericity of grain shape (i.e. $h \neq 1$) and from the differential damping and excitation along the direction parallel and perpendicular to the symmetry axis (i.e., $F_{\parallel} \neq F_{\perp}$, $G_{\parallel} \neq G_{\perp}$). For the disk-like grain, $\eta > 1$, the increase of $\langle \omega^2 \rangle$ is given by equation (8), and therefore we expect an increase of the frequency at the emission peak (hereafter peak frequency). Since the power radiated by a rotating grain is a nonlinear function of ω , we expect a substantial increase in the emissivity of spinning dust. We will study

⁴ The eigenvalues of the moment of inertia tensor of the disk of density ρ , radius R , and height L are $I_{\parallel} = \pi\rho R^4 L/2$, $I_{\perp} = (\rho\pi R^4 L/12)[3 + (L/R)^2]$.

TABLE 1
IDEALIZED ENVIRONMENTS FOR INTERSTELLAR MATTER

Parameters	CNM	WNM	WIM	RN	PDR
n_{H} (cm $^{-3}$)	30	0.4	0.1	10 3	10 5
T_{gas} (K)	100	6000	8000	100	1000
T_{d} (K)	20	20	20	40	80
χ	1	1	1	1000	30000
x_{H}	0.0012	0.1	0.99	0.001	0.0001
x_{M}	0.0003	0.0003	0.001	0.0002	0.0002
$y = 2n(\text{H}_2)/n_{\text{H}}$	0.	0.	0.	0.01	0.01

the correlation of the increase of peak frequency to the anisotropy in § 9.3.

Infrequent hits by single-ion collisions are able to transiently spin-up the grain, producing spikes of angular velocity ω . As a result, we expect both the peak frequency and total emissivity increase when the transient spin-up is taken into account. This issue we address in §8.

2.3. Idealized Environments

Table 1 presents physical parameters for idealized environments where n_{H} is the hydrogen number density, T_{gas} and T_{d} are gas and dust temperature, $\chi = u_{\text{rad}}/u_{\text{ISRF}}$ is the ratio of radiation energy density u_{rad} to the mean radiation density for the diffuse interstellar medium u_{ISRF} (see Mathis, Mezger, & Panagia 1983), $n(\text{H}_2)$, $n(\text{H}^+)$, $n(\text{M}^+)$ are the molecular hydrogen density, ion hydrogen density and ionized metal density, respectively. Physical parameters for the CNM, WNM, WIM, RN are similar to those in DL98b. The parameters for the PDR are taken to be similar to those inferred for the Orion Bar (see Allers et al. 2005).

3. ROTATIONAL DAMPING AND EXCITATION FOR IMPERFECT ALIGNMENT

Below we present calculations of rotational damping and excitation for a disk-like (or cylindrical) grain with principal moments of inertia I_{\parallel} and I_{\perp} . The disk has radius R and height L . The angular velocity ω is at an arbitrary angle with the grain symmetry axis \mathbf{a}_1 . When the angular velocity ω is not aligned with \mathbf{a}_1 , the rotation of the grain consists of the rotation about \mathbf{a}_1 with angular velocity ω_{\parallel} and the rotation about an axis perpendicular to \mathbf{a}_1 with angular velocity ω_{\perp} . Parallel and perpendicular components of dimensionless damping and excitation coefficients are defined as in equations (1) and (2), but I_{\parallel} , ω , τ_{H} are replaced by I_{\parallel} , ω_{\parallel} and $\tau_{\text{H},\parallel}$ and I_{\perp} , ω_{\perp} and $\tau_{\text{H},\perp}$.

3.1. Collisional Damping and Excitation

For a disk-like grain, the damping times for rotation parallel and perpendicular to the grain symmetry axis due to gas collisions are given in Appendix B. For a pure H gas of density n_{H} , they read

$$\tau_{\text{H},\parallel} \approx 4.12 \times 10^{10} a_{-7} \hat{\rho} T_2^{-1/2} \left(\frac{30 \text{ cm}^{-3}}{n_{\text{H}}} \right) \Gamma_{\parallel} \text{ s}, \quad (10)$$

$$\tau_{\text{H},\perp} \approx 4.58 \times 10^9 a_{-7} \hat{\rho} T_2^{-1/2} \left(\frac{30 \text{ cm}^{-3}}{n_{\text{H}}} \right) \Gamma_{\perp} \text{ s}, \quad (11)$$

$$\Gamma_{\parallel} \equiv \frac{8}{9} \left(\frac{6L}{R} \right)^{2/3} \frac{1}{(2L/R + 1)}, \quad (12)$$

$$\Gamma_{\perp} \equiv \left(\frac{4}{3} \right)^{1/3} \left(\frac{L}{R} \right)^{2/3} [3 + (L/R)^2] \times \frac{1}{g_{\perp}}, \quad (13)$$

where $\hat{\rho} \equiv \rho/2 \text{ g cm}^{-3}$, $T_2 \equiv T_{\text{gas}}/100 \text{ K}$, $a_{-7} \equiv a/10^{-7} \text{ cm}$, and

$$g_{\perp} = \frac{1}{6} \left(\frac{L}{R} \right)^3 + \frac{L}{R} + \frac{1}{2} \left(\frac{L}{R} \right)^2 + \frac{1}{2}. \quad (14)$$

For dimensionless collisional damping and excitation coefficients, $F_{\{\text{n},\text{i}\},\parallel} = F_{\{\text{n},\text{i}\},\perp}$ and $G_{\{\text{n},\text{i}\},\parallel} = G_{\{\text{n},\text{i}\},\perp}$ because they are normalized over those of purely H gas.

It is convenient to define components of thermal angular velocity parallel and perpendicular to the grain symmetry axis at the gas temperature T_{gas} :

$$\omega_{\text{T},\parallel} = \left(\frac{2k_{\text{B}}T_{\text{gas}}}{I_{\parallel}} \right)^{1/2}, \quad \omega_{\text{T},\perp} = \left(\frac{2k_{\text{B}}T_{\text{gas}}}{I_{\perp}} \right)^{1/2}. \quad (15)$$

3.2. Electric Dipole Damping

The electric dipole moment $\boldsymbol{\mu}$ of the grain is assumed to be fixed in the grain body system, and given by

$$\boldsymbol{\mu} = \mu_1 \mathbf{a}_1 + \mu_2 \mathbf{a}_2 + \mu_3 \mathbf{a}_3, \quad (16)$$

where μ_1 , μ_2 and μ_3 are components of $\boldsymbol{\mu}$ along the grain principal axes \mathbf{a}_1 , \mathbf{a}_2 and \mathbf{a}_3 , respectively.

The rotation of the electric dipole along \mathbf{a}_1 results in the damping for ω_{\parallel} , and its rotation along the axes perpendicular to \mathbf{a}_1 results in the damping for ω_{\perp} . The decrease of parallel and perpendicular components of angular velocity due to electric dipole emission are given by (see Appendix B3)

$$\frac{I_{\parallel} d\omega_{\parallel}}{dt} = -\frac{I_{\parallel}^2 \omega_{\parallel}^3}{3k_{\text{B}}T_{\text{gas}} \tau_{\text{ed},\parallel}}, \quad (17)$$

$$\frac{I_{\perp} d\omega_{\perp}}{dt} = -\frac{I_{\perp}^2 \omega_{\perp}^3}{3k_{\text{B}}T_{\text{gas}} \tau_{\text{ed},\perp}}, \quad (18)$$

where the damping times for rotation along and perpendicular to \mathbf{a}_1 are given by

$$\tau_{\text{ed},\parallel} = \frac{3I_{\parallel,\perp}^2 c^3}{6\mu_{\perp}^2 k_{\text{B}}T_{\text{gas}}}, \quad \tau_{\text{ed},\perp} = \frac{3I_{\parallel,\perp}^2 c^3}{6(\mu_{\parallel}^2 + \mu_{\perp}^2/2)k_{\text{B}}T_{\text{gas}}}, \quad (19)$$

and $\mu_{\parallel}^2 = \mu_1^2$ and $\mu_{\perp}^2 = \mu_2^2 = \mu_3^2 = \mu_{\perp}^2/2$ have been assumed.

Following DL98b, the dipole moment is given by

$$\mu^2 = 23 \left[\left(\frac{a_{\text{x}}}{a} \right)^2 \langle Z^2 \rangle + 3.8 \left(\frac{\beta}{0.4 \text{ D}} \right)^2 a_{-7} \right] a_{-7}^2 \text{ Debye}^2 \quad (20)$$

where $\langle Z^2 \rangle$ is the mean square grain charge, β is the dipole moment per atom of the grain, and $a_{-7} = a/10^{-7} \text{ cm}$. Plugging equation (20) into (19) with the assumption of uniform distribution of $\boldsymbol{\mu}$ along the grain principal axes, and using moments of inertia for the disk,

we obtain

$$\begin{aligned} \tau_{\text{ed},\parallel} &= \frac{3I_{\parallel}^2 c^3}{4\mu^2 k_{\text{B}} T_{\text{gas}}}, \\ &= 1.6 \times 10^{11} \rho^2 a_{-7}^8 \times \frac{(R/L)^{4/3}}{[(a_{\text{x}}/a)^2 \langle Z^2 \rangle + 3.8(\beta/0.4\text{D})^2 a_{-7}] T_2} \text{ s}, \end{aligned} \quad (21)$$

and

$$\begin{aligned} \tau_{\text{ed},\perp} &= \frac{3I_{\perp}^2 c^3}{4\mu^2 k_{\text{B}} T_{\text{gas}}}, \\ &= 4.0 \times 10^{10} \rho^2 a_{-7}^8 \times \frac{(R/L)^{4/3} (1 + \frac{1}{3}(L/R)^2)^2}{[(a_{\text{x}}/a)^2 \langle Z^2 \rangle + 3.8(\beta/0.4\text{D})^2 a_{-7}] T_2} \text{ s}. \end{aligned} \quad (22)$$

For grains larger than a_2 , $\tau_{\text{ed},\parallel} = \tau_{\text{ed},\perp}$.

3.3. Damping and Excitation by the Plasma

The problem of plasma-grain interactions for perfect internal alignment was studied in DL98b, and refined by Ali-Haïmoud et al. (2009). Here we consider the damping and excitation by the plasma for the case of imperfect internal alignment. We assume for simplicity that $\boldsymbol{\mu}$ is directed along \mathbf{a}_2 axis. We consider only neutral grain ($Z_{\text{g}} = 0$, as in DL98b), and assume a spherical grain with a cylindrical excitation equivalent radius a_{cx} (e.g. Ali-Haïmoud et al. 2009).

For an ionized gas with ion density n_i , ion mass m_i , and charge Z_i , the dimensionless excitation coefficients parallel and perpendicular to the grain symmetry axis from plasma drag are given by

$$G_{\text{p},\parallel,\perp} = \frac{n_i}{n_{\text{H}}} \left(\frac{m_i}{m_{\text{H}}} \right)^{1/2} \left(\frac{Z_i e \mu}{k_{\text{B}} T_{\text{gas}} a_{\text{cx}}^2} \right)^2 \frac{3}{2} \int_0^{\infty} u e^{-u^2} du g_{\parallel,\perp}, \quad (23)$$

where e is the elementary charge, $u \equiv v/v_{\text{T}}$, with v being the velocity and $v_{\text{T}}^2 \equiv 2k_{\text{B}}T_{\text{gas}}/m_i$, and

$$\begin{aligned} g_{\parallel,\perp} &= \int_{b_{\text{max}}/a_{\text{cx}}}^{\infty} \frac{dl}{l} \mathcal{I}_{\parallel,\perp} \left(\frac{u\Omega_{\parallel,\perp}}{l} \right), \\ \Omega_{\parallel,\perp} &= \left(\frac{m_i a_{\text{cx}}^2}{2k_{\text{B}} T_{\text{gas}}} \right)^{1/2} \omega_{\parallel,\perp}, \end{aligned} \quad (24)$$

where $\mathcal{I}_{\parallel,\perp}(u\Omega_{\parallel,\perp}/l)$ are given by equations (C12) and (C13) (see Appendix C2 for the definition of b_{max} and detailed calculations). Using the Fluctuation-Dissipation theorem (see Lazarian 1995; Lazarian & Roberge 1997 for the application to grain diffusion coefficients), we obtain $F_{\text{p},\parallel} = G_{\text{p},\parallel}$, and $F_{\text{p},\perp} = G_{\text{p},\perp}$.

Figure 1 presents $G_{\text{p},\parallel}$ and $G_{\text{p},\perp}$ for different values $\omega_{\parallel}/\omega_{\text{T},\parallel}$ and $\omega_{\perp}/\omega_{\text{T},\perp}$ for CNM. It can be seen that $G_{\text{p},\parallel}$ and $G_{\text{p},\perp}$ increase as the grain rotates slower, and for $\omega_{\parallel,\perp} < 10^{-3}$, they converge to the value for non-rotating grain, i.e. $\omega_{\parallel,\perp} = 0$.

4. PHOTOEXCITATION OF PAHS

Small PAHs are planar molecules, consisting of sp^2 -bonded C atoms in a two-dimensional hexagonal structure, with peripheric H atoms. PAHs absorb strongly

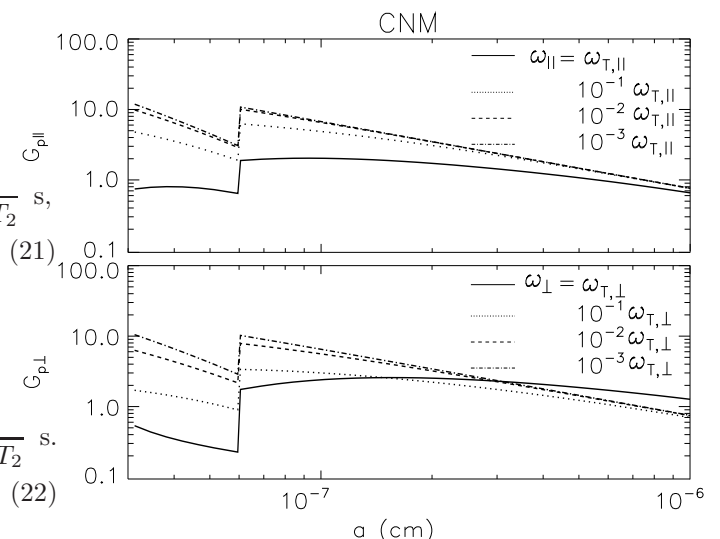


FIG. 1.— $G_{\text{p},\parallel}$ and $G_{\text{p},\perp}$ as function of a of a neutral grain for different values of $\omega_{\parallel}/\omega_{\text{T},\parallel}$ and $\omega_{\perp}/\omega_{\text{T},\perp}$ in the CNM. Electric dipole moment $\beta_0 = 0.4$ D is adopted.

in the ultraviolet. At wavelengths $3000 \lesssim \lambda \lesssim 1500 \text{ \AA}$, photoabsorption is primarily due to $\pi \rightarrow \pi^*$ electronic transitions, excited by electric fields parallel to the plane defined by the C atoms. PAHs – especially PAH ions – are also able to absorb at longer wavelengths, although the absorption is much weaker. The electronic transitions responsible for the absorption are not certain, but we will here assume that this absorption also involves transitions with electric dipole matrix elements parallel to the C atom plane.

Suppose the interstellar radiation field to consist of a unidirectional component providing a fraction γ of the local energy density of starlight, plus an isotropic component. Let $\hat{\mathbf{n}}_*$ be a unit vector parallel to the direction of propagation of the unidirectional component of the starlight. Let the dimensionless factor

$$U \equiv \frac{u_*}{u_{\text{MMP}}}, \quad (25)$$

where u_* is the starlight energy density, and $u_{\text{MMP}} = 6.85 \times 10^{-14} \text{ ergs cm}^{-3}$ is the estimate of Mathis, Mezger & Panagia (1983, hereafter MMP) for the local starlight energy density. Let $\dot{N}_{\text{abs},0}$ be the photon absorption rate for the PAH if illuminated by isotropic starlight with $U = 1$. Assuming the unidirectional and isotropic components to have similar spectra, the PAH photoexcitation rate is (Sironi & Draine 2009)

$$\dot{N}_{\text{abs}} = U \Psi(\theta) \dot{N}_{\text{abs},0}, \quad (26)$$

$$\Psi(\theta) \equiv \left[(1 - \gamma) + \gamma \frac{3}{4} (1 + \cos^2 \theta) \right], \quad (27)$$

$$\cos \theta \equiv \hat{\mathbf{n}}_* \cdot \mathbf{a}_1, \quad (28)$$

where \mathbf{a}_1 is a unit vector normal to the C atom plane.

5. REVISED ROTATIONAL EXCITATION AND DAMPING BY IR EMISSION

DL98b discuss the various processes contributing to the rotational excitation and deexcitation of very small dust grain. The dominant processes include direct collisions of atoms and ions with the dust grain, torques on the dust grain due to electric fields produced by passing

ions (“plasma drag”), and exchange of angular momentum with the electromagnetic field via absorption and emission of photons. Because a dust grain radiates many more photons than it absorbs, the emission processes are much more important than the change of angular momentum resulting from photon absorptions.

If the grain is rotating, then there will be a tendency for the infrared emission to, on average, reduce the grain angular momentum (Martin 1972). This process was included in the study by DL98b. As noted by Ali-Haimoud et al. (2009), the DL98b expression for the rotational damping torque from infrared emission was too small by a factor of two owing to an algebraic error. Here we make a more refined estimate of rates for excitation and deexcitation of PAH rotation due to infrared emission. We employ the PAH model of Draine & Li (2007, hereafter DL07); this grain model reproduces various observations of infrared emission, and therefore should provide an improved estimate of rotational excitation and damping from infrared emission. The present treatment also takes into account anisotropy in the infrared emission from planar PAHs.

Table 2 lists the character assumed for each of the vibrational modes in the DL07 PAH model.

TABLE 2
OPTICALLY-ACTIVE VIBRATIONAL MODES

$\lambda(\mu\text{m})$	in-plane fraction	identification*
3.30	1	C-H stretch
5.27	0	oop C-H bend overtone?
5.70	0	oop C-H bend overtone?
6.22	1	C-C stretch
6.69	1	C-C stretch
7.417	1	C-C stretch
7.598	1	C-C stretch
7.850	1	C-C stretch
8.33	1	ip C-H bend
8.61	1	ip C-H bend
10.68	0	oop mono C-H bend
11.23	0	oop mono C-H bend
11.33	0	oop mono C-H bend
11.99	0	oop duo C-H bend
12.62	0	oop trio C-H bend
12.69	0	oop trio C-H bend
13.48	0	oop quartet C-H bend
14.19	0	oop quartet C-H bend
15.90	2/3	?
16.45	2/3	?
17.04	2/3	?
17.375	2/3	?
17.87	2/3	?
18.92	2/3	?
15.	2/3	FIR continuum?

* ip = in-plane mode; oop = out-of-plane mode

Having in mind PAHs, we consider a grain with dynamical symmetry, with eigenvalues $I_1 > I_2 = I_3$ of the moment of inertia tensor. Let $\mathbf{a}_1, \mathbf{a}_2$ and \mathbf{a}_3 be unit vectors parallel to the principal axes corresponding to moments of inertia I_1, I_2 and I_3 , respectively. The vibrational modes will be assumed to have oscillations that are either parallel to \mathbf{a}_1 (“out-of-plane”) or perpendicular to \mathbf{a}_1 (“in-plane”). Let the angular momentum vector have components J_{\parallel} parallel to \mathbf{a}_1 , and J_{\perp} perpendicular

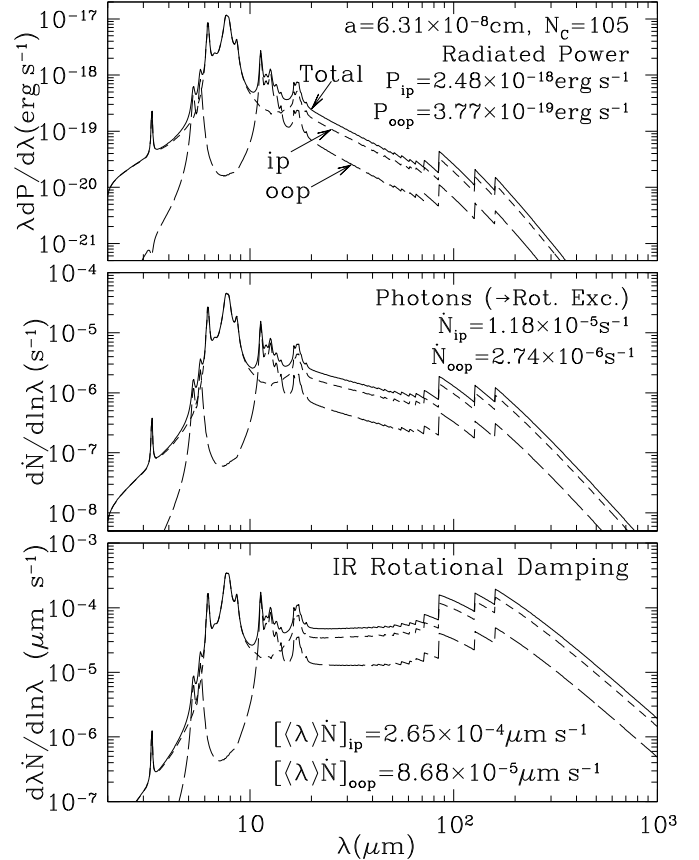


FIG. 2.— Moments of the infrared emission from a PAH ion with effective radius $a = 6.31 \text{ \AA}$ ($N_C = 105$ carbon atoms), heated by the average interstellar radiation field ($U = 1$). The radiated power (top panel) and photon emission rate (middle panel) are dominated by $5 \lesssim \lambda \lesssim 15 \mu\text{m}$ emission, but the rotational damping coefficient (bottom panel) has an appreciable contribution from emission out to $\lambda \approx 200 \mu\text{m}$. The sawtooth discontinuities in the spectra at $\lambda \gtrsim 50 \mu\text{m}$ arise from approximations in the calculational method (see text).

to \mathbf{a}_1 (i.e., in the \mathbf{a}_2 - \mathbf{a}_3 plane).

Suppose that the grain is absorbing photons at a rate \dot{N}_{abs} , and radiating photons with a power per unit frequency P_ν . For $U < 10^4$, small PAHs are in the single-photon-heating regime, with virtually all of the energy of an absorbed starlight photon being radiated before the next photon absorption occurs. This allows us to assume a universal time-averaged emission spectrum for each PAH, with the emission intensity proportional to the photon absorption rate:

$$P_{m,\nu} \approx U \Psi(\theta) P_{m,\nu,0}, \quad (29)$$

where $P_{m,\nu,0}$ is the time-averaged power per unit frequency radiated by in-plane ($m = ip$) or out-of-plane ($m = oop$) vibrations of a single PAH molecule or ion heated by isotropic radiation with $U = 1$. Figure 2 shows $\nu P_{m,\nu,0}$ for a PAH with $N_C = 105$ C atoms, where $P_{m,\nu,0}$ is obtained by solving the equations of statistical equilibrium for a PAH subject to stochastic heating (Draine & Li 2001, Li & Draine 2001b), using the “thermal-discrete” method, where the emission from a PAH at a given energy is estimated using a thermal approximation, but the downward transitions are treated as

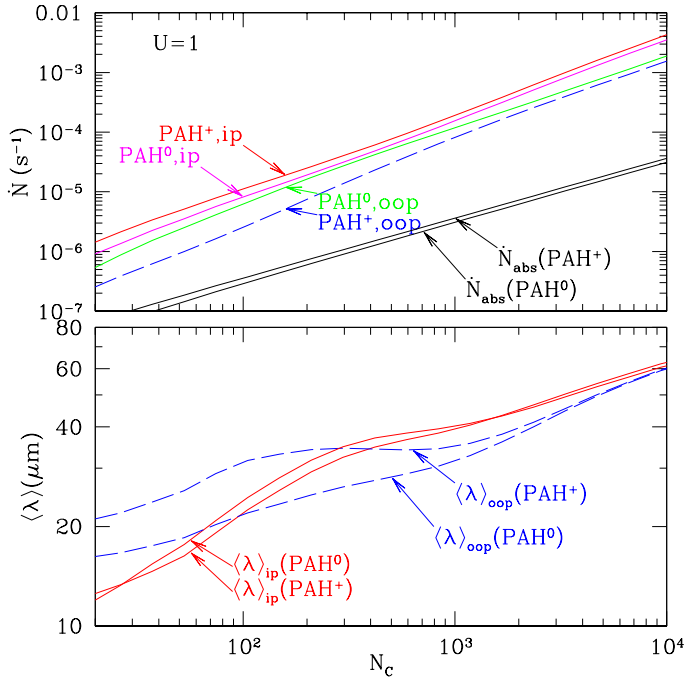


FIG. 3.— Rate of photon emission \dot{N} (upper panel) and $\langle \lambda \rangle$ (lower panel) as a function of N_C , the number of C atoms in the PAH, for PAHs in the local interstellar radiation field.

discrete transitions to a lower energy level. The model employs a heat capacity based on a realistic spectrum of vibrational modes (Draine & Li 2001), and updated vibrational band strengths (Draine & Li 2007) which, for a suitable PAH size distribution, closely reproduce observed IR spectra. The sawtooth discontinuities in the model spectrum arises from approximations in the treatment. The long-wavelength emission from a real PAH would presumably be dominated by a finite number of emission lines, but the continuous spectrum obtained here is expected to provide a reasonable representation for the distribution of emitted power over wavelength.

The photon emission rate

$$\dot{N}_m \approx U\Psi\dot{N}_{m,0}, \quad (30)$$

where

$$\dot{N}_{m,0} = \int_0^\infty \frac{1}{h\nu} P_{m,\nu,0} d\nu. \quad (31)$$

The middle panel of Figure 2 shows the integrand in eq. (31) for the time-averaged rate of photon emission \dot{N}_m by in-plane and out-of-plane modes, for PAH neutrals and ions.

The rotational damping also depends on the photon-weighted wavelength,

$$\langle \lambda \rangle_m \equiv \frac{1}{\dot{N}_m} \int_0^\infty \frac{\lambda}{h\nu} P_{m,\nu} d\nu, \quad (32)$$

for $m = ip$ or $m = oop$. The lower panel of Figure 2 shows the integrand in eq. (32). For the PAH emission properties assumed by Draine & Li (2007), the small fraction of the total power radiated at $\lambda \gtrsim 100\mu\text{m}$ contributes substantially to the integral in eq. (32), but does not dominate the integral.

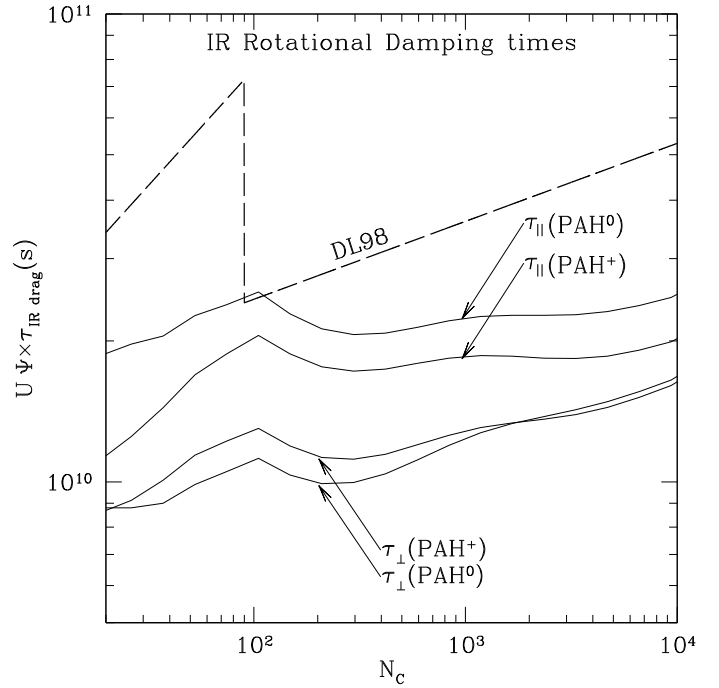


FIG. 4.— Time scale for damping of angular momentum parallel to the symmetry axis (J_{\parallel}) and perpendicular to the symmetry axis (J_{\perp}).

Figure 3 shows how \dot{N}_m and $\langle \lambda \rangle$ depend on the the number N_C of C atoms in the PAH.

Let J be the grain angular momentum. We assume that the grain has no intrinsic helicity, so that a nonrotating grain is equally likely to emit left- or right-circularly polarized photons. If the grain is initially non-rotating, IR emission will result in⁵

$$\left\langle \frac{dJ_{\parallel}}{dt} \right\rangle = \frac{1}{2} U\Psi(\theta) \left(\dot{N}_{\text{abs},0} + \dot{N}_{ip,0} \right) 2\hbar^2, \quad (33)$$

$$\left\langle \frac{dJ_{\perp}}{dt} \right\rangle = \frac{1}{2} U\Psi(\theta) \left[\dot{N}_{oop,0} + \frac{1}{2} \left(\dot{N}_{\text{abs},0} + \dot{N}_{ip,0} \right) \right] 2\hbar^2. \quad (34)$$

The infrared emission will, on average, remove angular momentum from the grain, with rates (see Appendix B2)

$$\left(\frac{dJ_{\parallel}}{dt} \right)_{\text{IR}} = -\frac{3\hbar}{2\pi I_{\parallel} c} U\Psi(\theta) \dot{N}_{ip,0} \langle \lambda \rangle_{ip} J_{\parallel}, \quad (35)$$

$$\left(\frac{dJ_{\perp}}{dt} \right)_{\text{IR}} = -\frac{3\hbar}{2\pi I_{\perp} c} U\Psi(\theta) \left[\frac{1}{2} \dot{N}_{ip,0} \langle \lambda \rangle_{ip} + \dot{N}_{oop,0} \langle \lambda \rangle_{oop} \right] J_{\perp}. \quad (36)$$

The characteristic time scales for rotational damping by IR emission are

$$\tau_{\text{IR},\parallel} \equiv \frac{-J_{\parallel}}{(dJ_{\parallel}/dt)_{\text{IR}}} = \frac{1}{U\Psi(\theta)} \frac{2\pi I_{\parallel} c}{3\hbar} \left[\dot{N}_{ip,0} \langle \lambda \rangle_{ip} \right]^{-1}, \quad (37)$$

$$\tau_{\text{IR},\perp} \equiv \frac{-J_{\perp}}{(dJ_{\perp}/dt)_{\text{IR}}} = \frac{1}{U\Psi(\theta)} \frac{2\pi I_{\perp} c}{3\hbar} \times \left[\left(\frac{1}{2} \dot{N}_{ip,0} \langle \lambda \rangle_{ip} + \dot{N}_{oop,0} \langle \lambda \rangle_{oop} \right) \right]^{-1}. \quad (38)$$

The rotational damping times $\tau_{\text{IR},\parallel}$ and $\tau_{\text{IR},\perp}$ are

⁵ The factor 2 in front of \hbar^2 is pointed out by Silsbee et al. (2010).

shown in Figure 4 for PAHs in the average interstellar radiation field. We show separate damping times for PAH⁰ and PAH⁺, but the timescale for changes in PAH ionization are short compared to the time scale for changes in angular momentum, so one should take an appropriate weighted mean:

$$\tau_{\text{IR},\parallel}^{-1} = f_0 \tau_{\text{IR},\parallel}^{-1}(\text{PAH}^0) + (1 - f_0) \tau_{\text{IR},\parallel}^{-1}(\text{PAH}^+), \quad (39)$$

$$\tau_{\text{IR},\perp}^{-1} = f_0 \tau_{\text{IR},\perp}^{-1}(\text{PAH}^0) + (1 - f_0) \tau_{\text{IR},\perp}^{-1}(\text{PAH}^+), \quad (40)$$

where f_0 is the neutral fraction for PAHs of that size.

Also shown is the rotational damping time estimated by DL98b for graphitic grains. Our new estimates for $\tau_{\text{IR},\parallel}$ and $\tau_{\text{IR},\perp}$ are smaller than the DL98b estimate by factors of 1–6, depending on size, charge state, and the orientation of \mathbf{a}_1 relative to the angular momentum \mathbf{J} . A factor of 2 is attributable to an algebraic error in DL98b (see Ali-Haimoud et al. 2009); the remaining differences are due to use of realistic PAH emission properties rather than the power-law heat capacity and power-law opacity used by DL98b, as well as different assumptions regarding the grain moment of inertia.

Using equations (1) and (2), the parallel and perpendicular components of the dimensionless coefficients of damping and excitation from infrared emission are then given by

$$F_{\text{IR},\parallel} = \frac{\tau_{\text{H},\parallel}}{\tau_{\text{IR},\parallel}}, \quad F_{\text{IR},\perp} = \frac{\tau_{\text{H},\perp}}{\tau_{\text{IR},\perp}}, \quad (41)$$

$$G_{\text{IR},\parallel} = \left\langle \frac{dJ_{\parallel}^2}{dt} \right\rangle \frac{\tau_{\text{H},\parallel}}{2I_{\parallel} k_{\text{B}} T_{\text{gas}}} \\ = \frac{1}{2} U \Psi(\theta) \frac{(\dot{N}_{\text{abs},0} + \dot{N}_{\text{ip},0}) 2\hbar^2}{2I_{\parallel} k_{\text{B}} T_{\text{gas}}} \tau_{\text{H},\parallel}, \quad (42)$$

$$G_{\text{IR},\perp} = \left\langle \frac{dJ_{\perp}^2}{dt} \right\rangle \frac{\tau_{\text{H},\perp}}{2I_{\perp} k_{\text{B}} T_{\text{gas}}} \\ = \frac{1}{2} U \Psi(\theta) \frac{[\dot{N}_{\text{oop},0} + \frac{1}{2}(\dot{N}_{\text{abs},0} + \dot{N}_{\text{ip},0})] 2\hbar^2}{2I_{\perp} k_{\text{B}} T_{\text{gas}}} \tau_{\text{H},\perp} \quad (43)$$

where I_{\parallel} and I_{\perp} are given by equation (A3).

The new coefficients for rotational excitation and damping by infrared emission derived in this section are compared with those from the DL98b model in Figures 5 and 6 for WIM, RN and PDR. There the electric dipole damping rate for parallel and perpendicular direction is also shown. For spherical grains (i.e. $a > 6 \times 10^{-8}$ cm), the parallel and perpendicular components of F_{IR} and G_{IR} are not the same as the electric dipole damping rate, i.e., there exists the anisotropy in the damping and excitation. Such a high anisotropy of the damping and excitation from infrared emission can result in important effects of the dynamics of spinning dust grains.

6. EFFECT OF GRAIN PRECESSION ON THE DIPOLE EMISSION

Earlier studies (DL98ab, Ali-Haimoud et al. 2009) assumed that the frequency of dipole emission from rotating grain is the same as the rotational frequency $\omega/2\pi$. Since the electric dipole is fixed in the body system, the rotation and precession of the grain with respect to fixed \mathbf{J} can induce some modification for the dipole emission frequency from its rotational frequency.

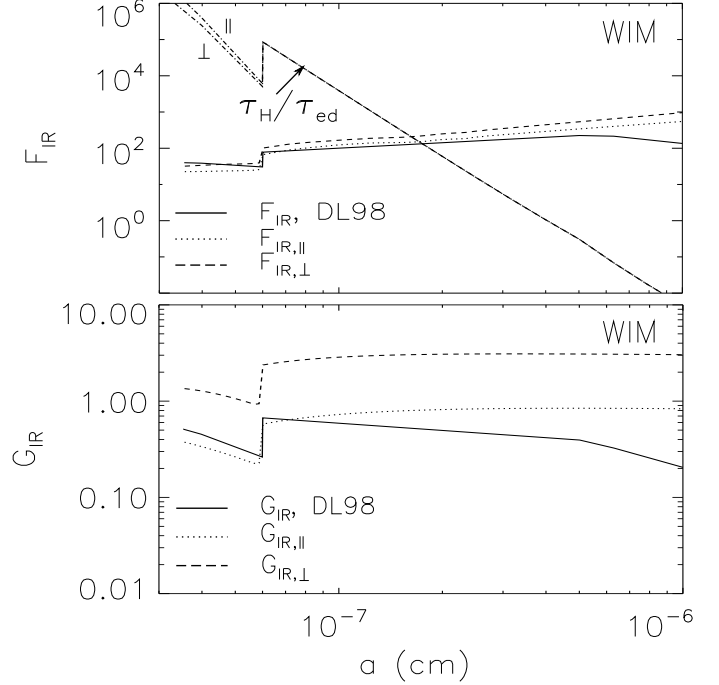


FIG. 5.— Comparison of our new damping and excitation coefficients arising from infrared emission, F_{IR} , G_{IR} with those in DL98b for WIM with $f_0 \approx 0$. The ratio of damping times $\tau_{\text{H}}/\tau_{\text{ed}}$ for rotation parallel and perpendicular to the grain symmetry axis also shown.

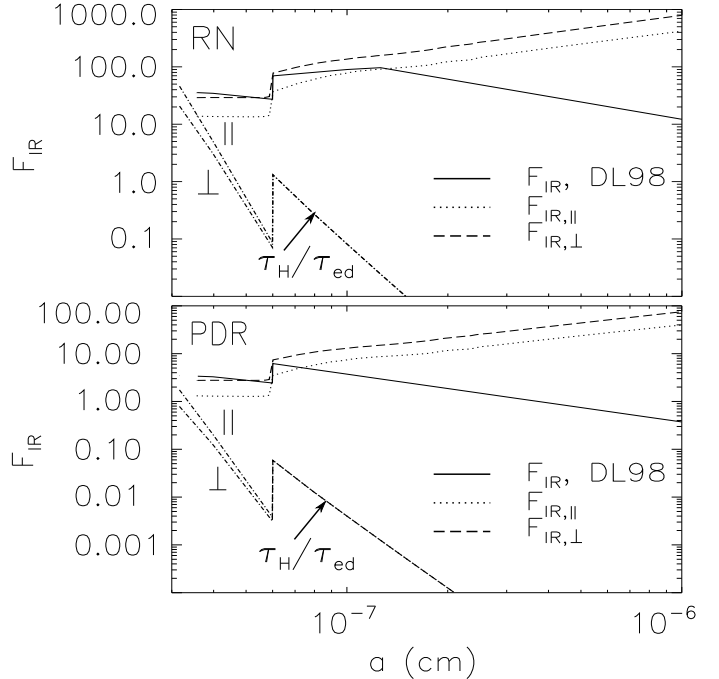


FIG. 6.— Similar to figure 5 but for RN and PDR. Here the neutral fraction of PAH $f_0 = 1$.

Let us consider the simple case of a disk-like grain where the dipole lies in the plane $\mathbf{a}_1 \mathbf{a}_2$:

$$\boldsymbol{\mu} = \mu_{\parallel} \mathbf{a}_1 + \mu_{\perp} \mathbf{a}_2 \quad (44)$$

in the grain body system. The torque-free motion of this grain with angular momentum \mathbf{J} and ratio of inertia moments h consists of the precession of the symmetry

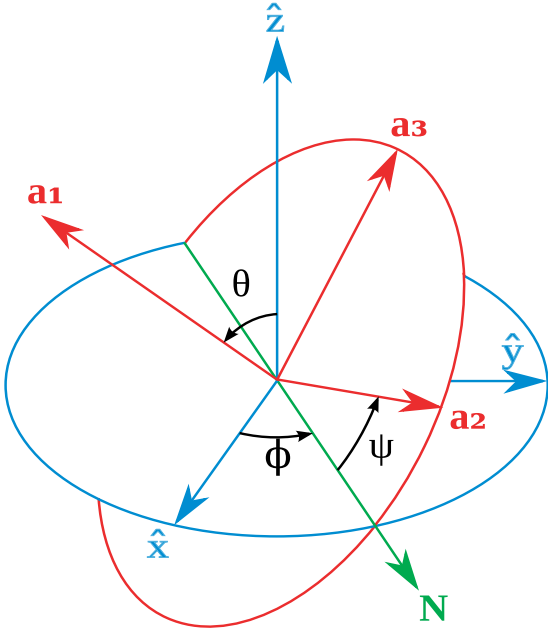


FIG. 7.— Torque-free motion of the grain in an external system with $\hat{\mathbf{z}} \parallel \mathbf{J}$ and $\hat{\mathbf{x}}, \hat{\mathbf{y}} \perp \mathbf{J}$ described by three Euler angles θ, ϕ and ψ .

axis \mathbf{a}_1 about \mathbf{J} with constant angle θ and rate $\dot{\phi}$, and the rotation of grain itself about the symmetry axis with the rate $\dot{\psi}$ where ϕ, ψ and θ are Euler angles (see Figure 7). The precession and rotation rates are respectively given by (Landau & Lifshitz 1976)

$$\dot{\phi} = \frac{J}{I_{\perp}}, \quad \dot{\psi} = (1-h) \frac{J}{I_{\parallel}} \cos \theta, \quad (45)$$

Precession and rotation of the grain with respect to \mathbf{J} results in an acceleration for the dipole moment:

$$\ddot{\boldsymbol{\mu}} = \mu_{\parallel} \ddot{\mathbf{a}}_1 + \mu_{\perp} \ddot{\mathbf{a}}_2, \quad (46)$$

where $\ddot{\mathbf{a}}_1$ and $\ddot{\mathbf{a}}_2$ are functions of time and given in Appendix F.

The instantaneous emission power of the dipole moment is defined by

$$P_{\text{ed}}(J, \theta, t) = \frac{2}{3c^3} |\ddot{\boldsymbol{\mu}}|^2. \quad (47)$$

The emission power of the grain is obtained by averaging (47) over the torque-free motion of the grain, i.e., over angles ψ and ϕ in the range from 0 to 2π . The final result for the case $\mu_{\parallel} = 0$ and $\mu_{\perp} = |\boldsymbol{\mu}|$ is

$$\frac{P_{\text{ed}}(J, \theta)}{2\mu_{\perp}^2/3c^3} = \frac{1 + \cos^2 \theta}{2} (\dot{\phi} + \dot{\psi})^4 - 2(\dot{\phi}^3 \dot{\psi} + \dot{\phi} \dot{\psi}^3) (1 - \cos \theta)^2 + \frac{1}{2} \dot{\psi}^4 \sin^2 \theta. \quad (48)$$

To find the frequency of dipole emission, we perform the Fourier transform for the components of dipole acceleration $\ddot{\boldsymbol{\mu}}$. Normalized square amplitude of the Fourier transform for the components $\ddot{\mu}_x$ (or $\ddot{\mu}_y$) and $\ddot{\mu}_z$ are shown in Figure 8 for $\theta = 15$ and 40° for a disk-like grain with $h = 1.5$. We can see that the emission spectrum from the electric dipole corresponds to three frequency modes, $\dot{\psi}/2\pi$, resulting from the component $\ddot{\mu}_z$, and $(\dot{\phi} \pm \dot{\psi})/(2\pi)$, arising from the component $\ddot{\mu}_x$ (or $\ddot{\mu}_y$).

The emission power from the former mode is negligible compared to that from the later modes, which have frequencies given by

$$\nu = \frac{\dot{\phi} \pm \dot{\psi}}{2\pi} = \frac{J}{I_{\parallel}} \frac{h \mp (h-1) |\cos \theta|}{2\pi}, \quad (49)$$

in which the major mode $(\dot{\phi} + \dot{\psi})/2\pi$ for $\theta < 90^\circ$ (or $(\dot{\phi} - \dot{\psi})/2\pi$ for $\theta > 90^\circ$) is much stronger than the second mode $(\dot{\phi} - \dot{\psi})/2\pi$ ($(\dot{\phi} + \dot{\psi})/2\pi$). When θ increases, the amplitude of higher frequency mode increases, and that mode becomes important as θ approaches 90° (see Fig. 8). However, for the fast internal relaxation, the angle θ fluctuates with small amplitude about \mathbf{J} , and the lower frequency mode is dominant. Therefore, we are interested only in the emission of this lower frequency mode in the present paper. The ratio of emission frequency of the dominant mode to the rotation frequency $\omega/2\pi$ is given by

$$\frac{\nu}{\omega/2\pi} = \frac{\dot{\phi} - |\dot{\psi}|}{\omega} = \frac{h - (h-1) |\cos \theta|}{\sqrt{\cos^2 \theta + h^2 \sin^2 \theta}} \leq 1. \quad (50)$$

It turns out that the dominant emission frequency is *smaller* than the rotation frequency, and it is very close to the rotation frequency for very small θ . The emissivity at the frequency ν per H is given by

$$\frac{j_{\nu}}{n_{\text{H}}} = \frac{1}{4\pi} \frac{1}{n_{\text{H}}} \int_{a_{\text{min}}}^{a_{\text{max}}} da \frac{dn}{da} j_{\nu,a}, \quad (51)$$

where

$$j_{\nu,a} = P_{\text{ed}}(J, \theta) f_{\nu}(J, \theta), \quad (52)$$

and $f_{\nu}(J, \theta) d\nu$ is the probability of the dipole emission in $[\nu, \nu + d\nu]$.

If we assume that all of the emission is at the dominant frequency given by (50), then equation (52) can be rewritten in terms of integrals over J and θ by introducing a Delta function:

$$j_{\nu,a} = \int \int d\theta dJ P_{\text{ed}}(J, \theta) \delta(\nu' - \nu) f_J f_{\theta}. \quad (53)$$

where $\nu' = \nu'(J, \theta)$ is the emission frequency corresponding to J and θ , $f_J dJ$ is the probability of the grain having angular momentum in $[J, J + dJ]$, and $f_{\theta} d\theta$ is the probability of the angle being in $[\theta, \theta + d\theta]$.

It is possible to calculate $j_{\nu,a}$ using (53). However, we can assume that the emission power is approximately given by a power law of the emission frequency

$$P_{\text{ed}}(\nu) = \frac{2}{3c^3} \frac{2}{3} \mu_{\perp}^2 (2\pi\nu)^4, \quad (54)$$

We found that the emissivity obtained using (51) and (52) with this approximation does not differ more than 10% from more rigorous calculations using (53). Therefore, in the following, we calculate the emissivity using equations (51-52) with the approximated emission power $P_{\text{ed}}(\nu)$ given by equation (54).

7. NUMERICAL METHODS

The most important element in calculating the emissivity from spinning dust grains is to find the probability

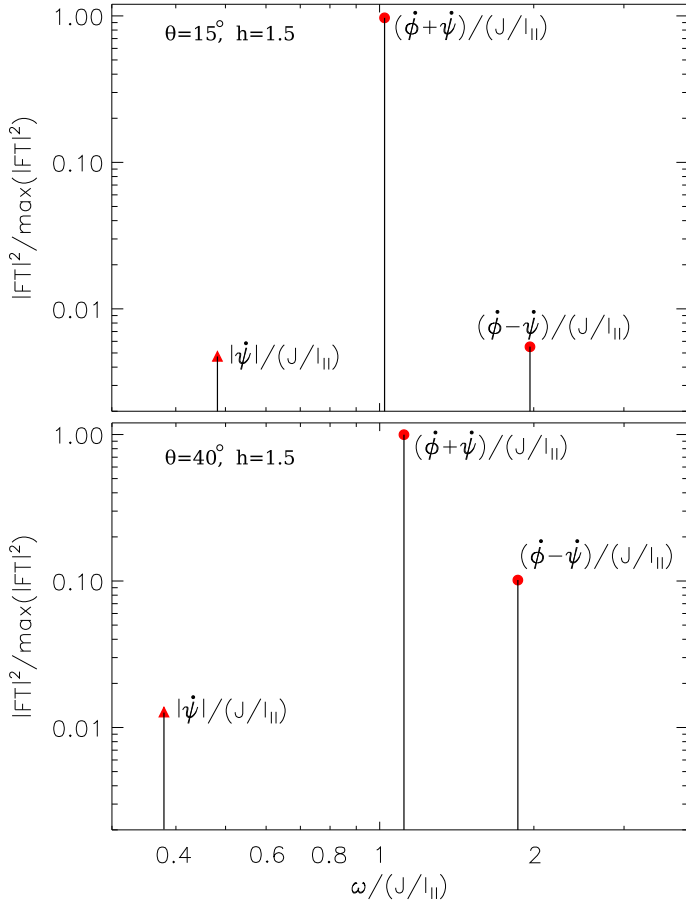


FIG. 8.— Normalized emission spectrum for a disk-like grain ($h = 1.5$) with $\mu_{\parallel} = 0$, for two values of the angle θ between the principal axis \mathbf{a}_1 and the angular momentum \mathbf{J} . The two components of $|\text{FT}(\dot{\mu}_x)|^2$ (or $|\text{FT}(\dot{\mu}_y)|^2$) are indicated by circles, while the component of $|\text{FT}(\dot{\mu}_z)|^2$ is indicated by a triangle.

distribution f_{ω} and f_{ν} for rotation resulting in emission at frequency ν for a given grain size a and a given electric dipole moment μ . Here we present a numerical approach using the Langevin equation to obtain those distribution functions.

7.1. The Langevin Equation

The Langevin equation is a well-known equation for describing stochastic dynamics (see Gardner 1983). In terms of its assumptions and applicability it is equivalent to the well known Fokker-Planck equation. In particular, the equation can handle only situations when the increments of the variable are smaller than the variable. Thus, the Langevin equation cannot be applied directly for treating the high impulse collisions of spinning dust grains with ions. Therefore in what follows we use a hybrid approach, describing the grain dynamics for most of the computational time using the Langevin equation and describing the infrequent (but high impact) collisions with ions as impulsive events.

The angular momenta of the impacting ions are drawn from distribution functions that include focusing by the attractive potential when approaching neutral or negatively-charged grains. For describing grain dynamics the Langevin equation was first suggested in Roberge, DeGraff & Flaherty (1993) and found more applications

in later works on grain alignment (see Roberge & Lazarian 1999, Hoang & Lazarian 2008, 2009).

7.1.1. 1D rotation

In an idealized situation when the grain rotates only about its axis of major inertia \mathbf{a}_1 , namely 1D rotation, the rotation of the grain is determined by the value of angular velocity $\omega \equiv \omega_{\parallel}$, and distribution function $f_{\nu} = 2\pi f_{\omega}$.⁶ Note that for this case, $\tau_{\text{H}} \equiv \tau_{\text{H},\parallel}$, and $\omega_{\text{T}} \equiv \omega_{\text{T},\parallel}$, and notations \parallel and \perp are omitted in this section.

For a given grain size, the evolution of ω can be described by a stochastic differential (Langevin) equation. In dimensionless units of $\omega' = \omega/\omega_{\text{T}}$ and $t' = t/\tau_{\text{H}}$, the Langevin equation reads

$$d\omega' = - \left[F_{\text{tot}}\omega' + \frac{2\omega'^3\tau_{\text{H}}}{3\tau_{\text{ed}}} \right] dt' + \sqrt{\frac{G_{\text{tot}}}{\tau_{\text{H}}}} dq, \quad (55)$$

where $dt' = dt/\tau_{\text{H}}$ is the time step, dq is a random variable with variance $\langle dq^2 \rangle = dt$, and the total damping F_{tot} and diffusion coefficients G_{tot} are given by

$$F_{\text{tot}} = F_i + F_n + F_{\text{IR}} + F_p, \quad (56)$$

$$G_{\text{tot}} = G_i + G_n + G_{\text{IR}} + G_p, \quad (57)$$

where F_j and G_j with $j=i, n, \text{IR}, p$ are damping and excitation coefficients corresponding to ion-grain, neutral-grain interactions, infrared emission and plasma drag.

To solve equation (55) for ω' , we numerically integrate it for N time steps with total time T . After each time step dt , the value ω' is updated via equation

$$\omega'_{i+1} = \omega'_i - \left[F_{\text{tot}}\omega'_i + \frac{2\omega_i'^3\tau_{\text{H}}}{3\tau_{\text{ed}}} \right] dt' + \sqrt{\frac{G_{\text{tot}}}{\tau_{\text{H}}}} dq, \quad (58)$$

for i running from 1 to N . The initial value ω'_0 is a random variable in the range $[0,1]$ generated from a uniform distribution function.⁷ The obtained solution ω'_i is binned and used to find the distribution function $f_{\omega}^{(1)}$. We note that $f_{\omega}^{(1)}$ is for the rotation along one axis only. By assuming isotropic distribution of the vector $\boldsymbol{\omega}$, the distribution function $f_{\omega} \propto \omega^2 f_{\omega}^{(1)}$ with normalization condition $\int_0^{\infty} f_{\omega} d\omega = 1$. Results for f_{ω} are presented in §7.3.

7.1.2. Grain Wobbling: 3D rotation

When the angular momentum is not completely aligned with the grain axis of major inertia (i.e., 3D rotation), its orientation within the grain body has to be accounted for in finding f_{ω} and f_{ν} .

Problems of internal alignment, i.e. to what extent the angular momentum J and the grain axis of major inertia are aligned have been always at the focus of the quantitative treatment of grain alignment (see Lazarian 2007, for a review). The initial works (e.g. Jones & Spitzer 1967) usually assumed a Maxwellian distribution for J . Then Purcell (1979) noticed that the internal relaxation of energy within a wobbling interstellar grain may be fast (i.e.,

⁶ This situation is similar that in the DL98 model and in the improved treatment by Ali-Haïmoud et al. (2009).

⁷ The initial value is unimportant as it is “forgotten” if the simulation is sufficiently long.

the timescale of internal relaxation is smaller compared to the gas damping time)⁸. Due to the fast internal relaxation demonstrated in Purcell (1979) for a period of time the works on grain dynamics assumed that the grain axis of major inertia must always be directed along the grain angular momentum, as this alignment minimizes the energy of the rotating grain. However, Lazarian (1994) noticed that this cannot be true for thermally rotating grains and restored the notion of grain wobbling as an essential element of grain dynamics.

In the 3D rotation case, we consider the evolution of \mathbf{J} in the lab coordinate system instead of $\boldsymbol{\omega}$. For a general grain shape, \mathbf{J} is completely determined by three components $J_{x,y,z}$ in the inertia coordinate system $\mathbf{e}_1\mathbf{e}_2\mathbf{e}_3$ (see Appendix E). The evolution of \mathbf{J} in time is also described by three Langevin equations

$$dJ_i = A_i dt + \sqrt{B_{ii}} dq_i, \text{ for } i = x, y, z, \quad (59)$$

where dq_i is the random Gaussian variables with $\langle dq_i^2 \rangle = dt$, $A_i = \langle \Delta J_i / \Delta t \rangle$ and $B_{ii} = \langle (\Delta J_i)^2 / \Delta t \rangle$ are damping and diffusion coefficients defined in the inertial coordinate system. In dimensionless units $\mathbf{J}' = \mathbf{J} / I_{\parallel} \omega_{T,\parallel}$, $t' = t / \tau_{H,\parallel}$, equation (59) becomes

$$dJ'_i = A'_i dt' + \sqrt{B'_{ii}} dq'_i, \quad (60)$$

where $\langle dq_i'^2 \rangle = dt'$, and

$$A'_i = -J'_i F_{\text{tot},\parallel} (\cos^2 \theta + \gamma_H \sin^2 \theta) - \frac{2}{3} \frac{J_i'^3}{\tau_{\text{ed}}'} \left(\cos^4 \theta + \gamma_{\text{ed}} \sin^4 \theta + \frac{h^3 + 3h}{2} \sin^2 \theta \cos^2 \theta \right) \quad (61)$$

$$B'_{ii} = \frac{B_{ii}}{2I_{\parallel} k_B T_{\text{gas}}} \tau_{H,\parallel}, \quad (62)$$

where

$$\tau_{\text{ed}}' = \frac{\tau_{\text{ed},\parallel}}{\tau_{H,\parallel}}, \quad \gamma_H = \frac{F_{\text{tot},\perp} \tau_{H,\parallel}}{F_{\text{tot},\parallel} \tau_{H,\perp}}, \quad \gamma_{\text{ed}} = \frac{I_{\parallel} \tau_{\text{ed},\parallel}}{I_{\perp} \tau_{\text{ed},\perp}}, \quad (63)$$

and θ is the angle between \mathbf{a}_1 and \mathbf{J} , $F_{\text{tot},\parallel}$, $F_{\text{tot},\perp}$ are total damping coefficients parallel and perpendicular to the grain symmetry axis, and B_{ii} are given in Appendix E.

7.2. Effect of Internal Thermal Fluctuations

Very little is known about internal relaxation in microscopic spinning grains. Thus, in what follows, for our description of grain wobbling we consider two extreme models. The first model assumes fast internal relaxation, with the distribution of deviations of the axis of grain maximal inertia from the direction of \mathbf{J} determined by the dimensionless ratio $J^2 / I_{\parallel} k_B T_d$, where T_d is the temperature of the grain body (Lazarian & Roberge 1997). The second model assumes no internal relaxation, with a Maxwellian distribution function for the angle between \mathbf{a}_1 with \mathbf{J} .

⁸ Purcell (1979) introduced a new magneto-mechanical effect, which he termed Barnett relaxation, which he showed to be able to align $0.1 \mu\text{m}$ grains over a time scale of the order of a year. Later another magneto-mechanical effect, termed nuclear relaxation, was introduced in Lazarian & Draine (1999). Nuclear relaxation is much faster than Barnett relaxation for $0.1 \mu\text{m}$ grains, but is not applicable to the tiny spinning grains considered here.

For a given value of angular momentum, and in the presence of fast internal relaxation, the angle θ between the grain axis of major inertia \mathbf{a}_1 and \mathbf{J} follows the local thermal equilibrium distribution function

$$f_{\text{LTE}}(\theta) = A \exp \left(-\frac{J^2}{2I_{\parallel} k_B T_d} (1 + [h - 1] \sin^2 \theta) \right), \\ = A \exp \left(-J'^2 \frac{T_{\text{gas}}}{T_d} (1 + [h - 1] \sin^2 \theta) \right), \quad (64)$$

where $h = I_{\parallel} / I_{\perp}$, $J' = J / I_{\parallel} \omega_{T,\parallel}$, and A is the normalization constant such that $\int_0^{\pi} f_{\text{LTE}}(\theta) 2\pi \sin \theta d\theta = 1$ (Lazarian & Roberge 1997).

When the timescale of internal relaxation is much longer than that of gas damping time, i.e., without internal relaxation, the angle distribution function is simply Maxwellian:

$$f_{\text{Mw}}(\theta) = \frac{h}{4\pi} \frac{1}{(\cos^2 \theta + h \sin^2 \theta)^{3/2}}, \quad (65)$$

where $\int_0^{\pi} f_{\text{Mw}}(\theta) 2\pi \sin \theta d\theta = 1$ (see Jones & Spitzer 1967; Lazarian & Roberge 1997).

To follow the evolution of \mathbf{J} in time in the presence of internal relaxation, we use the following algorithm. First, we generate initial values at $t = 0$ for J' , angle ξ between \mathbf{J} and \mathbf{e}_1 and azimuthal angle χ from uniform distribution functions. Thus, $J'_z(t = 0) = J' \cos \xi$, $J'_x(t = 0) = J' \sin \xi \cos \chi$ and $J'_y(t = 0) = J' \sin \xi \sin \chi$. Then we solve equations (60) with the time step dt to get J'_x , J'_y and J'_z and then J' at the moment $t + dt$. Due to the internal relaxation, the angle θ at that moment is unknown. Therefore, at the end of each timestep, θ is assumed to be a random angle generated from the distribution function (64, fast internal relaxation) or (65, without internal relaxation). With θ known, we can obtain the value of angular velocity $\omega_i = \sqrt{\omega_{\parallel}^2 + \omega_{\perp}^2}$ with its components $\omega_{\parallel} = (J / I_{\parallel}) \cos \theta$, and $\omega_{\perp} = (J / I_{\perp}) \sin \theta$. The dipole emission frequency of the dominant mode ν_i is calculated by (49). This process is repeated for N timesteps. The obtained value of angular velocity and dipole emission frequency at the end of each time step ω_i and ν_i are binned and will be used to find the distribution function f_{ω} and f_{ν} .

7.3. Benchmark Calculations

To benchmark our Langevin code, we first run simulations for the perfect internal alignment case to find $f_{\omega} = (1/2\pi) f_{\nu}$ to compare with the analytical distribution function obtained from the Fokker-Planck (FP) equation (Ali-Haïmoud et al. 2009). Physical parameters for different phases are given in Table 1. For very small PAHs, the dust temperature fluctuates due to transient heating by single photon. Therefore, we assume a smaller dust temperature $T_d = 10\text{K}$ for the CNM, WNM and WIM, and $T_d = 20$ and 40K for the RN and PDR, respectively, for smallest grains with $a < 7 \times 10^{-8}\text{cm}$. Rotational damping and excitation coefficients in Figure (20) are adopted for the benchmarks. We note that the results of LE simulations depend on the choice of right time step. Very small timesteps are inefficient, while large timesteps can introduce error. We define the

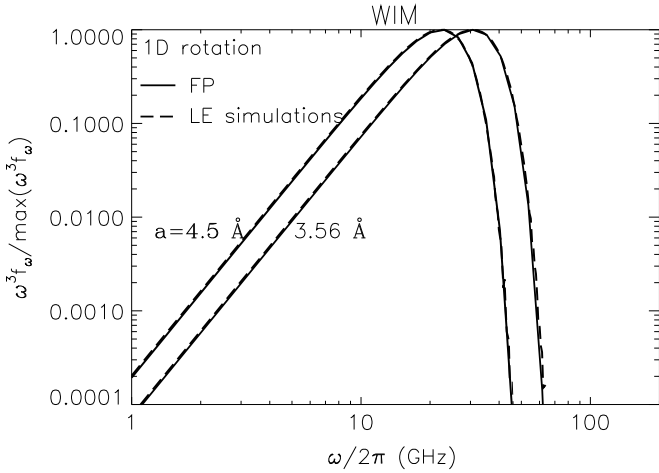


FIG. 9.— Comparison of normalized $\omega^3 f_\omega$ obtained from analytical solution of the FP equation and from numerical simulations of the Langevin equation for grain sizes $a = 3.56$ and 4.5 Å.

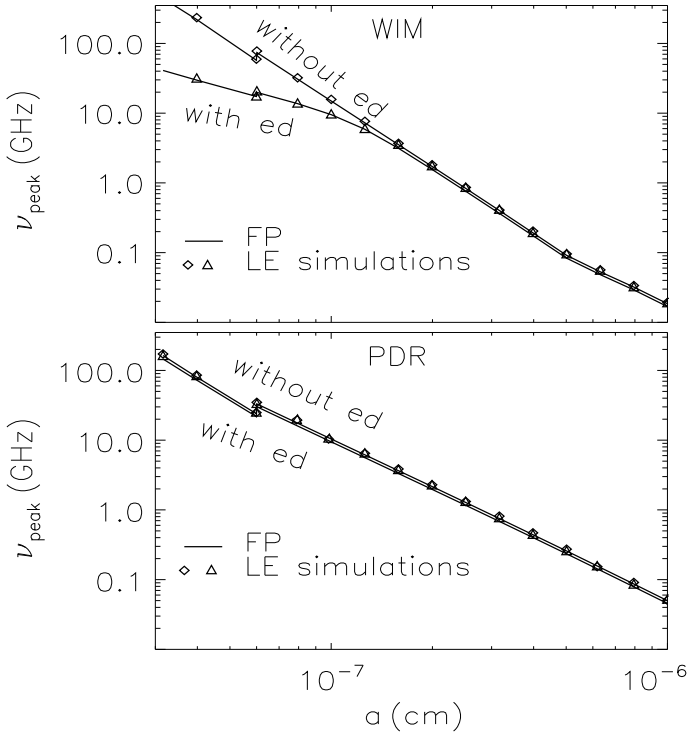


FIG. 10.— Comparison of peak frequency with and without electric dipole damping (ed) obtained from simulations of LE and FP for WIM (upper panel) and PDR (lower panel).

timestep by $dt = \epsilon \min[1/F_{\text{tot}}, 1/G_{\text{tot}}, \tau_{\text{H}}/\tau_{\text{ed}}]$. Our tests show that $\epsilon = 10^{-1}$ is a good choice. We run the LE simulations for $N = 10^7$ steps.

Figure 9 shows normalized $\omega^3 f_\omega$ for a grain with electric dipole moment parameter $\beta = \beta_0$ and sizes $a = 3.56$ and 4.5 Å obtained from the FP equation (solid lines) and the LE simulations (dashed lines) for the WIM.⁹ It can be seen that the LE simulations are in excellent agreement with analytical solutions of the FP equation.

Another important parameter we need to benchmark is the peak frequency as a function of grain size. For the

⁹ Hereafter, the distribution function f_ω for the case $\beta = \beta_0$ is presented.

perfect alignment case, the peak frequency is given by equation (160) in Ali-Haimoud et al. (2009). Using the distribution f_ω from LE simulations, we can obtain the peak frequency by maximizing the function $\omega^4 f_\omega$. Results from these two approaches are presented in Figure 10 for the WIM and PDR for both cases with and without electric dipole damping. In all cases, results from LE simulations coincide with those from the FP. For the PDR, the results with and without electric dipole damping are not much different because the electric dipole damping is negligible.

8. IMPULSIVE EXCITATION BY SINGLE-ION COLLISIONS

DL98b showed that for grains smaller than 7×10^{-8} cm, the angular impulse due to an individual ion-grain collision may be comparable to the angular momentum of the grain. Thus, infrequent hits of ions can result in transient rotational excitation for small grains.

Let τ_{icoll}^{-1} be the mean rate of ion collisions with the grain, given by

$$\tau_{\text{icoll}}^{-1} = f(Z_g = 0) n_i \pi a^2 \left(\frac{8k_B T_{\text{gas}}}{m_i \pi} \right)^{1/2} \left[1 + \frac{\sqrt{\pi}}{2} \Phi \right] + \sum_{Z_g \neq 0} f(Z_g) n_i \pi a^2 \left(\frac{8k_B T_{\text{gas}}}{m_i \pi} \right)^{1/2} g \left(\frac{Z_g Z_i e^2}{ak_B T_{\text{gas}}} \right), \quad (66)$$

where $\Phi = (2Z_i^2 e^2 / ak_B T_{\text{gas}})^{1/2}$, $g(x) = 1 - x$ for $x < 0$ and $g(x) = e^{-x}$ for $x > 0$, and $f(Z_g)$ is the grain charge distribution function (see Appendix D). The probability of the next collision occurring in $[t, t + dt]$ is

$$dP = \tau_{\text{icoll}}^{-1} \exp(-t/\tau_{\text{icoll}}) dt. \quad (67)$$

The rms angular momentum per ion collision (δJ^2) is inferred by dividing the total rms angular momentum to the collision rate, and its final formula is given in Appendix D.

The upper panel in Figure 11 presents the collision rate, τ_{icoll}^{-1} compared to the rate of electric dipole damping for the grain with $\beta = 0.4D$, τ_{ed}^{-1} , for the CNM, WNM and WIM. The effect of single-ion collisions is determined by the critical size a_{cri} corresponding to $\tau_{\text{icoll}}^{-1} = \tau_{\text{ed}}^{-1}$. For the WIM, it can be seen that for grains with $a \leq a_{\text{cri}} = 8.6 \times 10^{-8}$ cm, the electric dipole damping time is shorter than the time between two ion collisions. The active range of single-ion collisions for the WNM is $a \leq a_{\text{cri}} = 1.2 \times 10^{-7}$ cm. The critical size is smaller for the CNM with $a_{\text{cri}} = 3.8 \times 10^{-8}$ cm. Although, the single-ion collisions are important for the CNM, WNM and WIM, they are not important for the RN and PDR.

To account for single-ion collisions, we first use the Poisson distribution to generate the time intervals between successive collisions $\Delta\tau_{\text{icoll},j}$, which is a random variable in this case for a given τ_{icoll} . Thus, the n th collision occurs at the moment $t_{\text{icoll},n} = \sum_{j=1}^n \Delta\tau_{\text{icoll},j}$. We then run the integration for the LE (i.e., eq. 60) over time to find J and ω . The n th collision deposits an angular momentum $\Delta\mathbf{J}_n$ that is assumed to be randomly-oriented, with magnitude drawn from the distribution function with the rms $\langle \delta J^2 \rangle$ appropriate for the grain charge and radius. The impinging ions are taken to be protons for the WNM and WIM, and a mix of protons

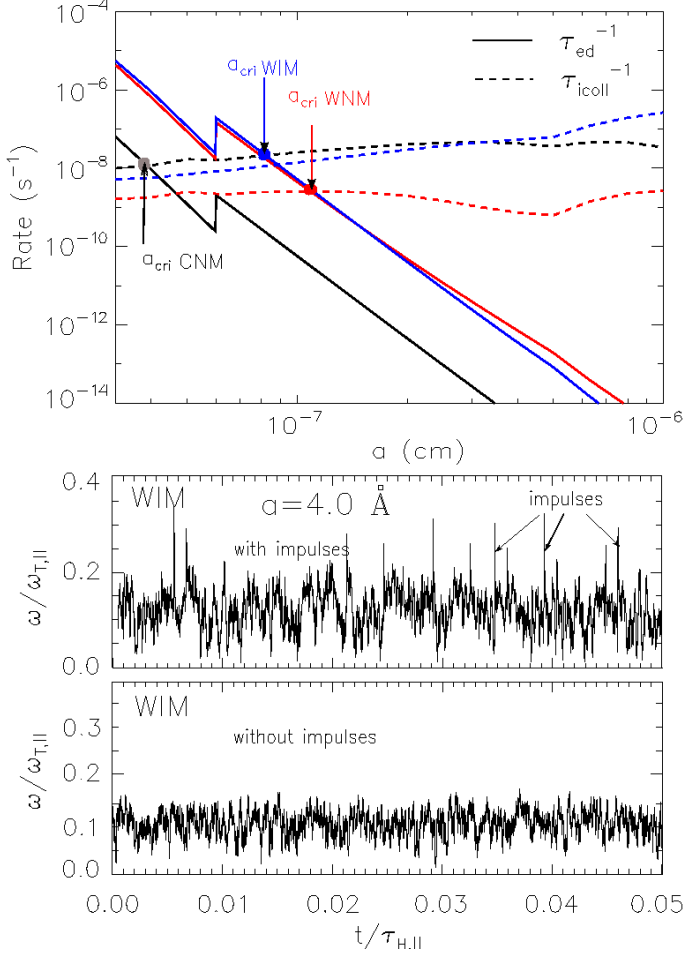


FIG. 11.— *Upper panel:* Comparison of ion collision rate τ_{icoll}^{-1} with the electric dipole damping rate τ_{ed}^{-1} of grains with electric dipole moment parameter $\beta = 0.4D$ for the CNM, WNM and WIM. The filled circle symbols denote the critical size a_{cri} when $\tau_{\text{icoll}}^{-1} = \tau_{\text{ed}}^{-1}$. *Lower panel:* The evolution of the angular velocity $\omega/\omega_{T,\parallel}$ as a function of $t/\tau_{H,\parallel}$ for the case with and without impulses from single-ion collisions in the WIM for $a = 4 \text{ \AA}$.

and C^+ ions, with fractional abundances x_{H} and x_{M} from Table 1, for the CNM. For the WIM and WNM in which the focusing effect due to negatively-charged grain is negligible, we can assume that the grain charge is given by the mean charge $\langle Z \rangle$. But for the CNM in which the focusing effect is important, we consider the grain in various charge states Z , and find the corresponding f_{ω} and f_{ν} .

To identify the role of single-ion collision on the distribution function, we first consider the perfect alignment case and solving 1D LE (Equation (55)). The resulting ω for the WIM is shown in the lower panel of Figure 11 for a grain size $a = 4 \text{ \AA}$. It can be seen that due to the electric dipole damping, the grain rotates subthermally most of the time with $\omega < \delta\omega$. Ionic impulses result in the transient rotational spin-up followed by the continuous damping by electric dipole emission.

Distribution functions obtained from LE simulations in the presence of impulses and the grain wobbling are compared with those when only the grain wobbling is considered (i.e., without impulses) in Figure 12 for the WNM (upper panel) and the WIM (lower panel) and for

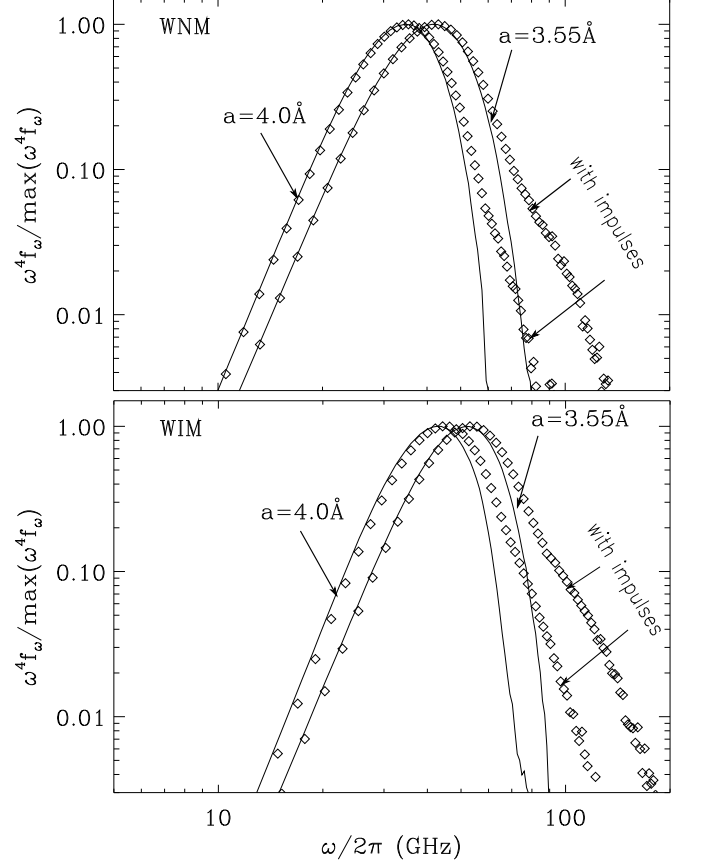


FIG. 12.— Normalized $\omega^4 f_{\omega}$ in the presence of impulses from single-ion collisions for the WNM (*upper panel*) and the WIM (*lower panel*) for two typical grain sizes. Impulses broaden the emission spectra to higher frequency (see diamond symbols).

two grain sizes 3.55 and 4.0 \AA . It can be seen that the ionic impulses extend the distribution function to higher frequency, but change only slightly the peak frequency of the spectrum. This effect is more important for smaller grains.

9. EMISSIVITY

Here we calculate the emissivity at the frequency ν using equation (51) with f_{ν} obtained from the LE simulations and the emission power $P_{\text{ed}}(\nu)$ from equation (54). To compare with earlier studies, we also calculate the emissivity using equation (3) with the Maxwellian distribution function f_{ω} from DL98b and the analytical distribution function from the FP equation (FP).

The emissivity is calculated assuming that 25% of the grains have the electric dipole moment parameter $\beta = 2\beta_0$, 50% have $\beta = \beta_0$ and 25% have $\beta = 0.5\beta_0$ with $\beta_0 = 0.4D$. The electric dipole moment μ is assumed to be isotropically distributed along the grain principal axes. We adopt the models of grain size distribution from Draine & Li (2007) with the total to selective extinction $R_{\text{V}} = 3.1$ and the total carbon abundance per hydrogen nucleus $b_{\text{C}} = 5.5 \times 10^{-5}$ for diffuse environments CNM, WNM and WIM, and $R_{\text{V}} = 5.5$, $b_{\text{C}} = 2.8 \times 10^{-5}$ for the RN and PDR for carbonaceous grains with $a_{\text{min}} = 3.55 \text{ \AA}$ and $a_{\text{max}} = 100 \text{ \AA}$.

9.1. Grain Wobbling: Imperfect Internal Alignment

Here we present our new calculations of emissivity accounting for imperfect internal alignment for the idealized environments listed in Table 1. We run simulations of LE (eq. 60) to find the distribution functions f_ν for 128 grain sizes in the range from a_{\min} to a_{\max} . For plasma drag and infrared emission, we use our new damping and excitation coefficients from Figures (1) and (5). For collisional damping and excitation, we use the results in DL98b as shown in Figure (20).

9.1.1. Distribution function f_ω

For a more instructive comparison of our results with earlier studies, here we present the distribution function of rotational frequency f_ω instead of the distribution function of dipole emission frequency f_ν , which is slightly different from the former one for the grains of the planar geometry.

Figure 13 shows normalized $\omega^4 f_\omega$ for the case of grain wobbling with and without fast internal relaxation, compared to that obtained using the FP method in Ali-Haïmoud et al. (2009) for a grain size $a = 4 \text{ \AA}$ for the WIM and PDR. To find the distribution function for the FP case, we use the parallel damping and excitation coefficients for the distribution function given by equation (34) in Ali-Haïmoud et al. (2009) because the grain is assumed to rotate along the symmetry axis.

It can be seen that in both environments, the grain wobbling results in a higher peak frequency, and the entire distribution functions are shifted to higher frequencies. Furthermore, the distribution function for the case without internal relaxation is extended to higher frequency than that with fast internal relaxation because the higher rotation frequency in the later case corresponds to higher internal dissipation rate of energy (see dotted line in the lower panel).

9.1.2. Emissivity

We calculate the emissivity per H using the distribution function f_ν found in the previous subsection for different environments in the presence of fast internal relaxation and without internal relaxation.

In Figure 14, we compare our results in the presence of fast internal relaxation with those obtained using methods in DL98b and Ali-Haïmoud et al. (2009) for perfect internal alignment for the WIM and RN. The parallel damping and excitation coefficients are taken in use to find the distribution function for the later cases.

First, it can be seen that the grain wobbling results in increases of the peak frequency. Compared to results from the FP equation method in Ali-Haïmoud et al. (2009), we see that the peak frequency increases from $\sim 23 \text{ GHz}$ to $\sim 33 \text{ GHz}$ for the WIM and from ~ 106 to $\sim 161 \text{ GHz}$ for PDR. Also, the peak emissivity of spinning dust in the later case is increased by factors of ~ 1.5 for the WIM and ~ 1.8 for PDR, respectively.

The emissivity per H for various idealized environments are summarized in Figure 15 with and without fast internal relaxation, respectively. The solid lines denote the emission spectra for the case of fast internal relaxation. The shaded areas represent the expected spectra when the internal relaxation varies from fast to very slow. The subplot represents $j_\nu/j_{\nu,FP}$ with j_ν and $j_{\nu,FP}$ being the emissivity at the peak of the emission spectrum for

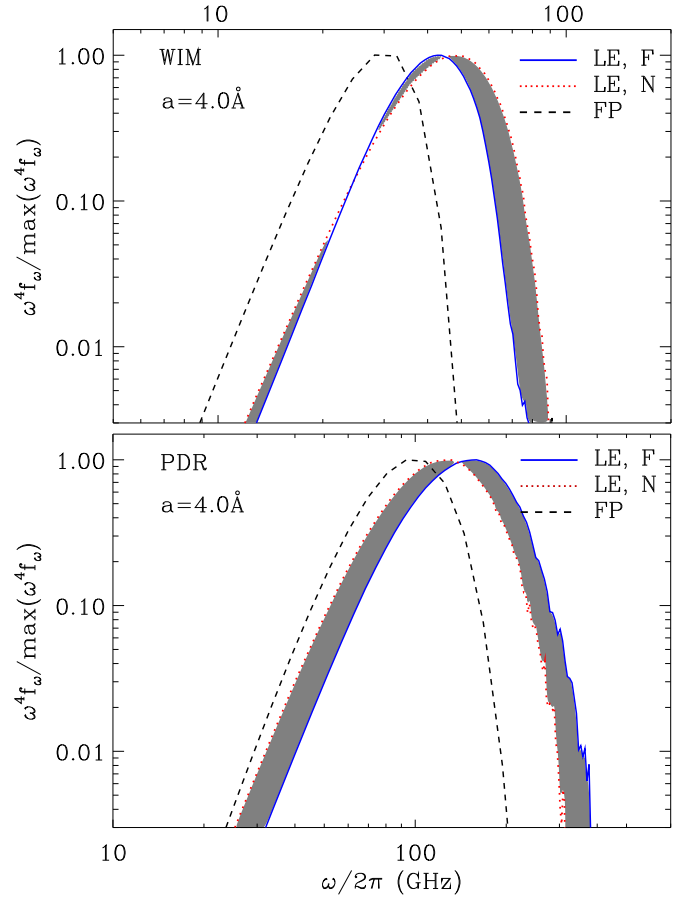


FIG. 13.— Comparison of normalized $\omega^4 f_\omega$ for the case of perfect internal alignment using the FP method (dashed line, FP) in Ali-Haïmoud et al. (2009) with that in the presence of grain wobbling obtained from simulations of LE, both with fast internal relaxation (LE, F) and without internal relaxation (LE, N). Shading areas denote the transition from fast internal relaxation (solid line) to without internal relaxation (dot line). For both the WIM and PDR, the peak frequency of distribution function increases, and the spectrum shifts to higher frequency in the later cases.

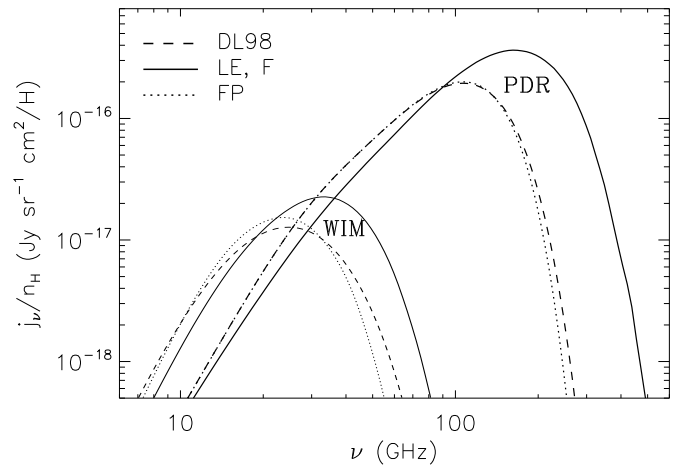


FIG. 14.— Comparison of emissivity spectrum for the grain wobbling (solid line) with those from the 1D rotation case (dot and dashed lines) and the fast internal relaxation (LE, F) is taken into account. The peak frequency of WIM increases from ~ 23 to $\sim 33 \text{ GHz}$ and its increases from ~ 106 to $\sim 161 \text{ GHz}$ for PDR, relative to that from the FP equation method in Ali-Haïmoud et al. (2009). Emissivity increased by a factor of ~ 1.5 and 1.8 for WIM and PDR, respectively.

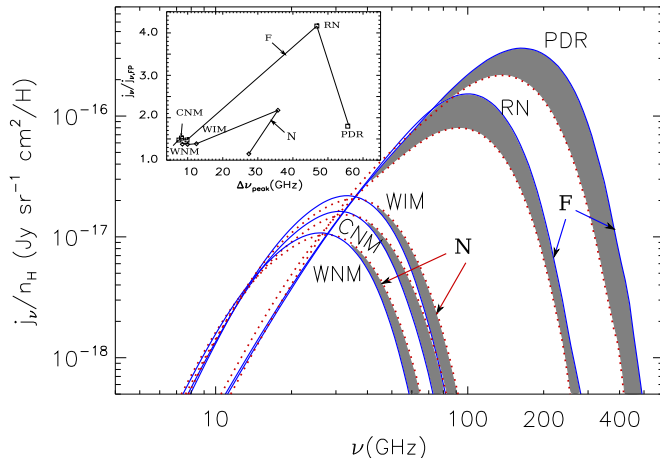


FIG. 15.— Emissivity per H in the case of grain wobbling for various environments. Gray shaded areas represent the transition between fast internal relaxation (F, solid lines) to no internal relaxation (N, dot lines). Subplot shows $j_\nu/j_{\nu,FP}$ with $j_{\nu,FP}$ being the peak emissivity from the method of FP equation, as a function of the increase of peak frequency $\Delta\nu_{\text{peak}}$ for fast internal relaxation (F) and no internal relaxation (N).

the imperfect alignment case and that from the FP equation method, as a function of the increase in the peak frequency $\Delta\nu = \nu_{\text{peak}} - \nu_{\text{peak,FP}}$ of emission spectrum.

Figure 15 shows that the increase of emissivity and peak frequency for the grain wobbling case is important. The peak frequency is increased from 8 to 55 GHz (i.e., by factors of 1.2 to 1.8) different environments (see subplot in Figure 15). The peak emissivity is increased by factors 1.47 (1.42), 1.5 (1.4), 1.52 (1.37), 1.8 (1.2) for WNM, WIM, CNM and PDR, respectively, corresponding to the cases with fast internal relaxation (without internal relaxation), except for the RN where the peak emissivity enhancement can reach a factor of 4.1(2.2) (see the subplot). In addition, the enhancement of peak frequency for the case without internal relaxation is smaller than that for fast internal relaxation. That can be explained by the fact that some emissivity from its peak can be transferred to higher frequency, resulting more extended spectra present in the case without internal relaxation (dot line in Figure 15).

The highest increase of peak emissivity present in the RN seems difficult to explain. We note that for this medium, the infrared damping and excitation is the most important process. Therefore, in addition to the anisotropy due to the non-spherical geometry, the anisotropy in the damping and excitation due to IR emission results in such a substantial increase of peak emissivity and peak frequency (see equation 8). The correlation of the increase of peak frequency and emissivity with the anisotropy for the grain wobbling case will be investigated in §9.3.

9.2. Emissivity in the Presence of Single-Ion Collisions

To see the effect of single-ion collision on the emissivity of spinning dust, consider first the case of perfect alignment. We are interested only in the CNM, WNM and WIM where the single-ion collisions are important.

We run the LE simulations for the grain wobbling taking into account the impulses for grain size from a_{min} to a_{cri} for these environments. We consider both the fast internal relaxation and without internal relaxation. The

resultant emissivity is compared with that from the case without impulses in Figure 16 for the WNM and WIM.

It can be seen that the ionic impulses broaden efficiently the emission spectra to the higher frequency, but they change slightly the peak frequency. For the WIM, the net effect of impulses and grain wobbling enhances the peak emissivity by a factor of 1.73, and the peak frequency is increased from ~ 23 to ~ 35 GHz. The corresponding increase in peak emissivity for the WNM is a factor of 1.58, and the peak frequency is increased from ~ 19 to ~ 27 GHz. By subtracting the effect of grain wobbling, we see that the impulses can increase the peak emissivity by $\sim 23\%$ and 11% for the WIM and WNM, respectively, but they increase slightly the peak frequency (see Figures 15 and 16).

For the CNM, the lower panel of Figure 17 shows that the effect of impulses on the total emissivity is weaker than for the WIM and WNM. The reasons for that are as follows. First, although the focusing effect is important for the grain in the negatively charged state, resulting in rotational impulses at high frequency (see the dot line in the upper panel of Figure 17), the probability of the grain in this negative charge state is relatively small. Second, since the effective range of impulses of the CNM is much narrower than that for the WIM and WNM (see the upper panel of Figure 11), its emissivity, that is obtained by integrating over the entire grain size distribution, is obviously less affected by impulses compared to the WIM and WNM.

We note that for a small grain in the CNM, WNM and WIM, during a short interval of several t_{icoll} , the grain experiences some rotational spikes due to single-ion collisions as shown in the left lower subplot of Figure 11. The peak frequency and width of the spectrum are related to the mean square value, $\langle\omega^2\rangle$, which is averaged over total integration time T . Therefore, the overall effect of the transient spin-up is to broaden the emission spectrum and increase the total emissivity as seen in Figure 16.

9.3. Effect of the non-sphericity and anisotropy in rotational damping and excitation

To understand why the grain wobbling induces the substantial increase of peak frequency and emissivity found in the previous sections, let us consider a disk-like grain shape and when internal relaxation is important.

To investigate the effect of grain wobbling for both spherical grains ($a > a_2$) and disk-like grain ($a < a_2$), we run LE simulations to find f_ω and ν_{peak} for the case of imperfect internal alignment assuming fast internal relaxation, for grain size from a_{min} to a_{max} .

We consider here the RN and PDR for which electric dipole damping is subdominant. Results are shown in Figure 18 where solid and dashed lines represent ν_{peak} obtained using the DL98 model and LE simulations, respectively. The ratio of ν_{peak} to that of DL98 model is depicted in the upper right subplot.¹⁰ The excitation anisotropy ratio $\alpha_{\parallel}/\alpha_{\perp}$ (see eq. 9) is shown in the lower left subplot.

First of all, for the PDR, the peak frequency from LE simulations is slightly higher than that from the DL98 model for spherical grains ($a > a_2 = 6 \times 10^{-8}$ cm). For

¹⁰ When the electric dipole damping is negligible, the distribution f_ω is Maxwellian, therefore $\nu_{\text{peak,FP}} \equiv \nu_{\text{peak,DL98}}$

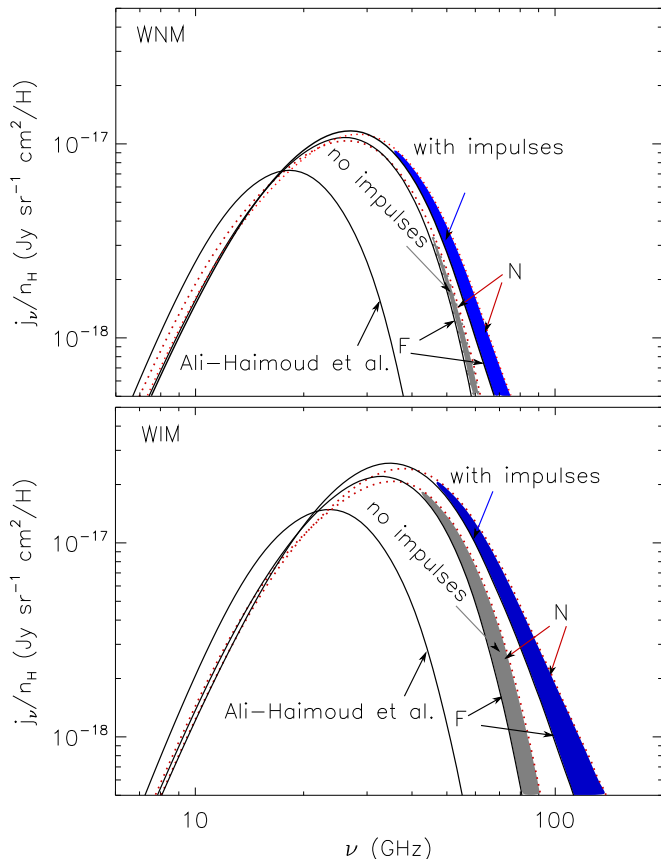


FIG. 16.— Emissivity per H obtained for the WNM (upper panel) and WIM (lower panel) without ionic impulses using the FP, and with impulses using our LE simulations for grain wobbling. The spectra are efficiently broadened as a result of impulses. Fast internal relaxation is more efficient at highest frequency, resulting in narrower spectra compared to those for the case without internal relaxation (red color line).

very small disk-like grains ($a < 6 \times 10^{-8}$ cm), the peak frequency is increased by a mean factor of ~ 1.5 . For the RN, one interesting feature is that the peak frequency from LE is much larger than that from the DL98 model for spherical grains (cf. to the PDR). We attribute the increase to the anisotropy in the grain rotational damping and excitation due to the infrared emission, which is the most important process of grain excitation for the RN. For spherical grains in the range from a_2 to 10^{-7} cm, η increase from 1.2 to 1.4 for the PDR, and from 1.8 to 2.3 for the RN (see subplots in the lower left corner of Figure 18). Hence, the higher anisotropy in the RN corresponds to the higher increase of peak frequency compared to the PDR case.

To see clearly the dependence of the increase in ν_{peak} in the grain wobbling case, we plot $\nu_{\text{peak}}/\nu_{\text{peak,DL98}}$ as a function of η for the PDR in Figure 19. The solid line corresponds to

$$\frac{\nu_{\text{peak}}}{\nu_{\text{peak,DL98}}} \approx \sqrt{\frac{\langle \omega^2 \rangle}{\langle \omega^2 \rangle_{\text{DL98}}}} = \sqrt{\frac{2\eta + 1}{3}} \quad (68)$$

where diamonds show ν_{peak} from the LE simulations. We see that the ratio $\nu_{\text{peak}}/\nu_{\text{peak,DL98}}$ increases with η as expected. For small η , ν_{peak} from the LE simulations is similar to that from equation (68), and some difference appears when η increases (see Figure 18). This may stem

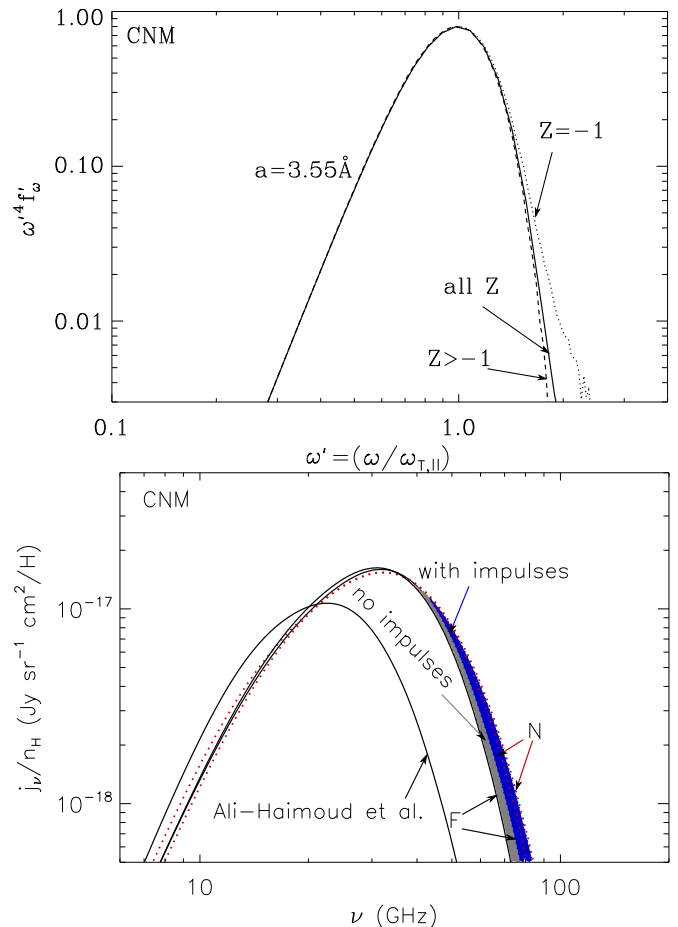


FIG. 17.— Effect of impulses due to single-ion collisions for the CNM: normalized $\omega'^4 f'_\omega$ with f'_ω is the normalized distribution function, as a function of $\omega' = \omega/\omega_{T,\parallel}$ where Z is the grain charge Z (upper panel) and emissivity (lower panel). Gray and blue shaded areas correspond to the transition between fast internal relaxation (solid line) and without internal relaxation (dot line) for the case without and with impulses, respectively. The focusing effect for the grain with charge $Z = -1$ enhances the high-frequency tail (dot line in upper panel)

from two reasons. First, the angular velocity distribution function f_ω for $\eta \sim 1$ is Maxwellian, but it differs from the Maxwellian distribution when η increases. Second, the assumption that $\omega_{x,y,z}$ are independent in deriving equation (68) is not valid because they have complex motion in the inertial coordinate system.

In other words, the anisotropy due to non-sphericity of grain shapes *and* the anisotropy in the grain rotational damping and excitation both act to increase the peak frequency of the emission.

Finally, we note that the total emissivity due to spinning dust scales as $\omega^4 f_\omega$, thus, the increase of ν_{peak} naturally is accompanied by the increase of the peak emissivity as observed in Figure 15.

10. DISCUSSION

10.1. Comparison with earlier studies

The DL98 model was the first proposal to explain the 20 – 40 GHz anomalous foreground emission in terms of rotational emission from ultra-small dust particles. Numerous observations (Dobler et al. 2009 and references therein) have confirmed the DL98 model predictions.

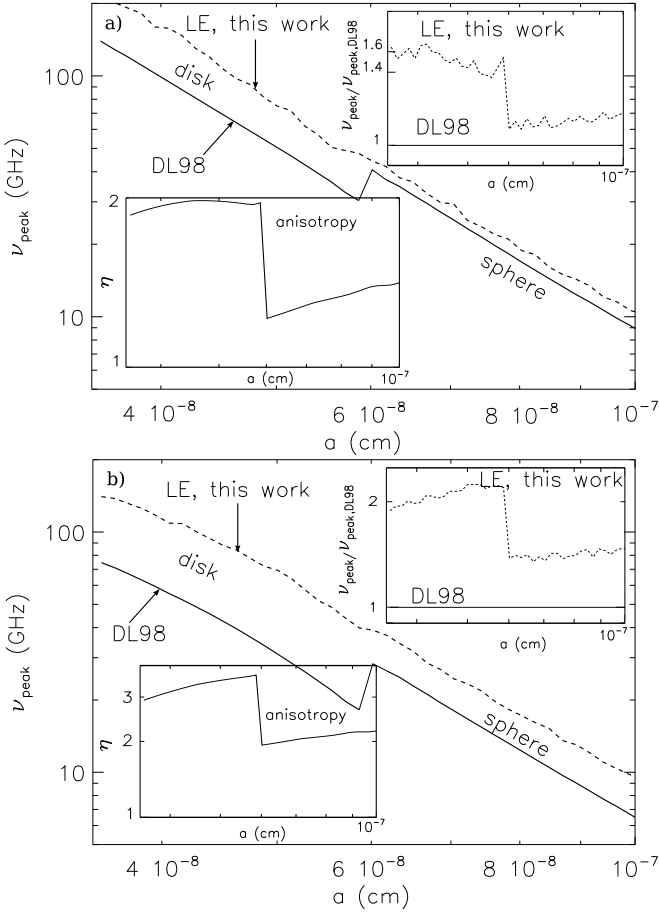


FIG. 18.— Peak frequency as a functions of grain size for the PDR (a) and RN (b). Dashed and solid lines denote the result obtained from LE simulations ν_{peak} , and from the DL98 model $\nu_{\text{peak,DL98}}$, respectively. The ratio $\nu_{\text{peak}}/\nu_{\text{peak,DL98}}$ versus a is shown in the upper corner subplot, and the anisotropy $\eta = \alpha_{\parallel}/\alpha_{\perp}$ is shown in the left lower corner.

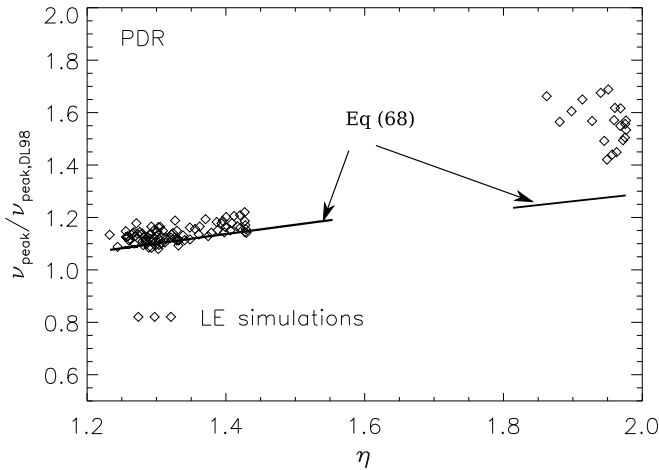


FIG. 19.— The ratio of peak frequency $\nu_{\text{peak}}/\nu_{\text{peak,DL98}}$ as a function of anisotropy η obtained from LE compared to the ideal case (eq. 68) for the PDR. The gap between $\eta = 1.4$ and 1.8 arises from the change in the grain geometry from sphere to disklike.

In the DL98 model the calculations were mostly analytical. The present study used a different approach, namely, the Langevin equation. We successfully benchmarked our calculations against the Fokker-Plank calculation in Ali-Haïmoud et al. (2009) for the perfect alignment case, and then introduced additional effects not included in DL98. In particular, our approach allows us to treat discrete high impact impulses arising from single-ion collisions with the grain. Most importantly, it enables us to study the spinning dust emission for the case of imperfect internal alignment with and without fast internal relaxation.

Among grain rotational damping and excitation processes, plasma drag is shown to be important for Molecular Clouds and CNM. Ragot (2002) considered the interactions of the plasma with spinning dust from the point of view of generation of waves. We believe that for the case we consider, the dust-plasma interaction is accurately approximated by interaction of the grain with individual, uncorrelated, passing ions.

DL98b noted that the typical rotational quantum number of even a small PAH would be $J/h \gtrsim 10^2$, allowing the dynamics to be treated classically. Ysard & Verstraete (2009) formulated the problem quantum-mechanically; the close correspondence between their results and those of DL98b confirms that a classical treatment is entirely adequate.¹¹

While our studies confirm the general validity of the DL98 model of spinning dust emission, they also show ways of making the model predictions more accurate. For instance, our refined treatment of grain dynamics provides peak emissivity predictions which differ by factors from ~ 2 to 4 from the original ones, depending on the environments. These differences may be detectable with high precision future observations.

The largest uncertainty within the model is the value of the dipole electric moment. The distribution of dipole moments adopted in DL98b was only an educated guess. Moreover, this distribution could be affected by interstellar processes and change from one media to another. For instance, Dobler et al. (2009) showed the anomalous emission in the 5-year WMAP data exhibits a bump at ~ 40 GHz. This peak frequency is larger than the prediction by the original DL98b model but could be explained if a modified distribution of electric dipole moments is adopted (Dobler et al. 2009), but the new effects considered here – misaligned rotation and impulsive excitation by ions may also explain the observed emission spectrum.

10.2. Effect of single-ion collisions

DL98b pointed out that for the CNM, WNM and WIM the angular momentum transferred in a single ion collision can be larger than the angular momentum of the rotating grain, but neither DL98b or the subsequent paper by Ali-Haïmoud et al. (2009) treated the impulsive nature of the ion collisions.

In the present paper, we describe ion-grain collisions as Poisson-distributed discrete events. When an ion hits the grain surface, the grain undergoes transient spin-up and then gets damped, mainly by electric dipole damp-

¹¹ In discussing some effects, e.g., dust-plasma interactions, DL98b did include quantum limitations for the angular momentum transfer, i.e. that ΔJ cannot be less than \hbar .

ing. Due to strong electric dipole damping, small grains spend most of their time rotating subthermally between two rotational spikes due to single-ion collisions. Ionic impulses are shown to be important for grains smaller than $\sim 8.6 \times 10^{-8}$, 1.2×10^{-7} and 3.8×10^{-8} cm for the WIM, WNM and CNM, respectively. Our quantitative simulations show that the impulses extend the high-frequency tail of the emission spectrum but change the peak frequency only slightly. They can enhance the peak emissivity by 23% and 11% for the WIM and WNM, respectively.

10.3. *Effect of Grain Wobbling*

The DL98b model assumed perfect alignment of the grain axis of maximal moment of inertia with the instantaneous angular momentum. This assumption is valid only for strong internal relaxation *and* suprathermal (much faster than thermal) rotation of grains (Lazarian 1994). The tiny grains we deal with rotate thermally or subthermally. For such a rotation, the grain axes are *not* coupled with the angular momentum. Due to imperfect internal alignment (i.e., grain wobbling), the anisotropy arising from grain shape, and differential damping and excitation (e.g. due to infrared emission and plasma drag) obviously affect the grain mean rotation rate and therefore the emissivity. Increased grain anisotropy, as measured by the anisotropy ratio η (eq. 9) produces an increase in the peak frequency and emissivity.

As we do not know the rates for internal relaxation in microscopic molecular size grains, we considered two cases: very rapid internal relaxation, and very slow internal relaxation. Using the Langevin equation, we showed that for the former case, the peak emissivity of spinning dust increases by a factor of ~ 2 , and the peak frequency of the spectrum increases by factors from 1.4 to 1.8, depending on the environment. Grain wobbling has a larger effect in broadening the emission spectrum when the internal relaxation is slow. Especially, for the RN when the anisotropy of damping and excitation from infrared emission is very high, the peak emissivity can be increased by a factor of 4 and peak frequency is increased by a factor of 2.

For the WIM, the joint effect of grain wobbling and impulses due to single-ion collisions causes the peak frequency to shift from ~ 23 to ~ 35 GHz. It is interesting to note that the new predicted peak frequency is close to the bump with the anomalous emission found in the WMAP five year data (Dobler et al. 2009). In their paper, using the DL98b model, they explained the observed spectrum with a modified model of spinning dust in which the grains have broader distribution of electric dipole moments. They also varied the number density of the WIM to produce spectra with higher peak frequency. These modifications do not seem to be necessary with our improved treatment of grain dynamics.

11. SUMMARY

The present paper provides a refinement of the DL98 model of spinning dust emission. Our principal results are outlined below:

1. We derived the rotational damping and excitation coefficients arising from plasma drag, infrared emission, gas drag and the electric dipole damping for small disk-like grains with imperfect internal alignment.

2. A nonspherical grain precessing around its angular momentum \mathbf{J} radiates primarily at two frequency modes. The lower frequency is dominant and is not the same as the rotational frequency $\omega/2\pi$.

3. Using the Langevin equation, we calculated the emissivity of grains with disaligned rotation, both with and without fast internal relaxation. For fast internal relaxation, allowing for disaligned rotation, the peak emissivity of spinning dust is increased by a factor ~ 2 for the CNM, WNM, WIM and PDR; and by a factor of ~ 4 for the RN, compared to those from the FP equation method. Fast internal relaxation also shifts the emission spectra to higher frequencies factors of 1.4 to 2 for these environments. Slow internal relaxation broadens the emission spectrum and reduces the enhancement in the peak emissivity.

4. The increase of peak emissivity and frequency of spinning dust in the grain wobbling case compared to those from the DL98 model has two sources: the anisotropy of the moment of inertia tensor, and the anisotropy in the rotational damping and excitation processes (e.g. infrared emission and plasma drag). Higher anisotropy results in higher enhancement of peak frequency and emissivity.

5. We devised a method to include the high-impact ion collisions within our statistical treatment of grain rotation. We found that for the CNM, WNM and WIM, single-ion impulses result in strong broadening of the emission spectrum to higher frequency and increases the emissivity of spinning dust. Impulsive excitation is most efficient for the WIM, but it is not important for the RN and PDR. In all idealized environments, the transient spin-up is subdominant compared to grain wobbling in terms of enhancement of emissivity, but it is dominant in spectrum broadening for the CNM, WNM and WIM.

6. For the WIM, the net effect of grain wobbling and transient spin-up from single-ion collision increases the peak emissivity by a factor ~ 1.7 , and the peak frequency increases from ~ 23 to ~ 35 GHz. That increase in peak frequency brings the model into agreement with the 5-year WMAP data without modifying the electric dipole momentum distribution or number density of the WIM as was proposed by Dobler et al. (2009).

TH and AL acknowledge the support of the Center for Magnetic Self-Organization and the NSF grant AST 0507164. BTB acknowledges partial support from NSF grant AST 0406883. BTB is grateful to Chris Hirata for helpful discussions, and to R.H. Lupton for availability of the SM graphics program.

APPENDIX

A. GRAIN PROPERTIES

A1. Grain shape and size

Here we present grain model and assumptions, notations we use throughout the paper. Grains are assumed to be disklike with radius R and height L for size $a < a_2$ and spherical for $a \geq a_2$. We chose $a_2 = 6 \times 10^{-8}$ cm as in DL98b. The “surface-equivalent” radius a_s and the “excitation equivalent” radius a_x of the grain were defined in DL98b.

Ali-Haïmoud et al. (2009) defined the radius of cylinder with the same $\int r^2 \sin^2 \theta dS$ with $r \sin \theta$ is the distance from the grain surface to the symmetry axis, thus

$$4\pi a_{\text{cx}}^4 \equiv \frac{3}{2} \oint r^2 \sin^2 \theta dS. \quad (\text{A1})$$

The expressions for a_s , a_x and a_{cx} are given in DL98b and Ali-Haïmoud et al. (2009). We adopt the models of grain size distribution from Draine & Li (2007) with the total to selective extinction $R_V = 3.1$ and the total carbon abundance per hydrogen nucleus $b_C = 5.5 \times 10^{-5}$ for diffuse environments CNM, WNM and WIM, and $R_V = 5.5$, $b_C = 2.8 \times 10^{-5}$ for the RN and PDR for carbonaceous grains with $a_{\text{min}} = 3.55 \text{ \AA}$ and $a_{\text{max}} = 100 \text{ \AA}$.

A2. Moments of Inertia

Consider a PAH with N_C carbon atoms, plus peripheral H atoms that make a minimal contribution to the total mass. We take the surface density of C atoms in a planar PAH to be that in a single plane of graphite: $\sigma_C = 3.7 \times 10^{15} \text{ C cm}^{-2}$. We will assume that PAHs with $N_C < N_1$ consist of a monolayer, but larger PAHs will be multilayered, with number density of C atoms $n_C = 1.1 \times 10^{23} \text{ cm}^{-3}$. We approximate the PAH as a disk of radius R and height L , with

$$L = \frac{\sigma_C}{n_C} \left[1 + A \max(0, N_C^{1/3} - N_1^{1/3}) \right], \quad R^2 = \frac{N_C}{\pi n_C L} \quad (\text{A2})$$

Neglecting the contribution of the H atoms, the moments of inertia are

$$I_{\parallel} = N_C m_C \frac{R^2}{2}, \quad I_{\perp} = N_C m_C \left(\frac{R^2}{4} + \frac{L^2}{12} \right), \quad (\text{A3})$$

We take $N_1 = 10^2$ and $A = 0.4$; with this choice, the PAH consists of two layers when $N_C = 364$.

B. ROTATIONAL DAMPING

Gas-grain interactions, plasma-grain interactions, infrared emission, and radio emission damp the rotation of small grains. In this section we present the rates for these processes.

We consider a disk-like grain with temperature T_d in gas of temperature T_{gas} , H nucleon density $n_{\text{H}} = n(\text{H}) + 2n(\text{H}_2)$, and with $n(\text{He}) = 0.1n_{\text{H}}$. Following DL98, we “normalize” the various drag processes to the drag which would be produced by “sticky” collisions in a pure H gas of density n_{H} : thus for drag process j , we define the dimensionless quantity $F_{j,\parallel,\perp}$ corresponding to the rotational damping parallel and perpendicular to the symmetry axis \mathbf{a}_1 , such that the contribution of process j to the drag torque is

$$I_{\parallel,\perp} \left(\frac{d\omega_{\parallel,\perp}}{dt} \right)_j \equiv - \left(\frac{I_{\parallel,\perp} \omega_{\parallel,\perp}}{\tau_{\text{H},\parallel,\perp}} \right) F_{j,\parallel,\perp}. \quad (\text{B1})$$

For the disk-like grain in a pure hydrogen gas of density n_{H} , $F_{j,\parallel,\perp} = 1$, and the damping times for rotation along and perpendicular to its symmetry axis are given by

$$\tau_{\text{H},\parallel} = \frac{3I_{\parallel}}{4\pi a_{\text{cx}}^4 n_{\text{H}} m_{\text{H}} (2k_{\text{B}} T_{\text{gas}} / \pi m_{\text{H}})^{1/2}}, \quad \tau_{\text{H},\perp} = \frac{3I_{\perp}}{\pi R^4 n_{\text{H}} m_{\text{H}} (2k_{\text{B}} T_{\text{gas}} / \pi m_{\text{H}})^{1/2} g_{\perp}}, \quad (\text{B2})$$

where

$$g_{\perp} = \frac{1}{6} \left(\frac{L}{R} \right)^3 + \frac{L}{R} + \frac{1}{2} \left(\frac{L}{R} \right)^2 + \frac{1}{2}. \quad (\text{B3})$$

Using standard parameters for the interstellar diffuse medium (ISM) and moments of inertia I_{\parallel}, I_{\perp} for the disk, we get

$$\tau_{\text{H},\parallel} \approx 4.12 \times 10^{10} \hat{\rho} a_{-7} T_2^{-1/2} \left(\frac{30 \text{ cm}^{-3}}{n_{\text{H}}} \right) \Gamma_{\parallel} \text{ s}, \quad \text{and} \quad \tau_{\text{H},\perp} \approx 4.58 \times 10^9 \hat{\rho} a_{-7} T_2^{-1/2} \left(\frac{30 \text{ cm}^{-3}}{n_{\text{H}}} \right) \Gamma_{\perp} \text{ s}, \quad (\text{B4})$$

where $\hat{\rho} \equiv \rho/2 \text{ g cm}^{-3}$, $T_2 \equiv T_{\text{gas}}/100 \text{ K}$, $a_{-7} \equiv a/10^{-7} \text{ cm}$, where $a \equiv (3/4)^{1/3} L^{1/3} R^{2/3}$, and

$$\Gamma_{\parallel} = \frac{8}{9} \left(\frac{6L}{R} \right)^{2/3} \frac{1}{[2L/R + 1]}, \quad \Gamma_{\perp} = \left(\frac{4}{3} \right)^{1/3} \left(\frac{L}{R} \right)^{2/3} [3 + (L/R)^2] \times \frac{1}{g_{\perp}} \quad (\text{B5})$$

We will use $\tau_{H,\parallel,\perp}$ as a fiducial time scales for the different sources of rotational damping. Thus the rotational damping times due to process j are

$$\tau_{j,\parallel,\perp}^{-1} = F_{j,\parallel,\perp} \tau_{H,\parallel,\perp}^{-1}. \quad (\text{B6})$$

The linear drag processes are additive:

$$F_{\parallel,\perp} = F_{n,\parallel,\perp} + F_{i,\parallel,\perp} + F_{p,\parallel,\perp} + F_{\text{IR},\parallel,\perp}, \quad (\text{B7})$$

where F_n , F_i , F_p , and F_{IR} are the contributions from neutral impacts, ion impacts, plasma drag, and thermal emission of infrared photons.

B.1. Plasma Drag

For a grain with an electric dipole moment $\boldsymbol{\mu}$, the interaction of this electric dipole moment with passing ions in the plasma results in a damping and excitation (Anderson & Watson 1993). The damping due to this process is obtained using the Fluctuation Dissipation theorem, i.e., $F_{p,\parallel,\perp} = G_{p,\parallel,\perp}$ with $G_{p,\parallel,\perp}$ are derived in Appendix C2.

B.2. Rotational Damping by IR Emission

Let \mathbf{a}_2 , \mathbf{a}_3 , \mathbf{a}_1 be axes fixed in the grain. Consider an oscillator with dipole moment

$$\boldsymbol{\mu} = \mu_2 \mathbf{a}_2 \cos \omega_0 t = \frac{\mu_2}{2} [(\mathbf{a}_2 \cos \omega_0 t + \mathbf{a}_3 \sin \omega_0 t) + (\mathbf{a}_2 \cos \omega_0 t - \mathbf{a}_3 \sin \omega_0 t)]. \quad (\text{B8})$$

Now consider rotation of the grain around \mathbf{a}_1 with angular velocity ω_r :

$$\mathbf{a}_2 = \hat{\mathbf{x}} \cos \omega_r t + \hat{\mathbf{y}} \sin \omega_r t, \quad \mathbf{a}_3 = \hat{\mathbf{y}} \cos \omega_r t - \hat{\mathbf{x}} \sin \omega_r t, \quad (\text{B9})$$

where $\hat{\mathbf{x}}$, $\hat{\mathbf{y}}$, $\hat{\mathbf{z}}$ define an inertial coordinate system. The dipole moment is

$$\boldsymbol{\mu} = \frac{\mu_2}{2} [\hat{\mathbf{x}} \cos(\omega_r + \omega_0)t + \hat{\mathbf{y}} \sin(\omega_r + \omega_0)t + \hat{\mathbf{x}} \cos(\omega_r - \omega_0)t + \hat{\mathbf{y}} \sin(\omega_r - \omega_0)t], \quad (\text{B10})$$

i.e., a dipole $(\mu_2/2)$ rotating with frequency $(\omega_0 + \omega_r)$, plus a dipole $(\mu_2/2)$ rotating retrograde with frequency $(\omega_0 - \omega_r)$. The net loss of angular momentum is

$$\Gamma = - \left[\frac{2(\mu_2/2)^2 (\omega_r + \omega_0)^4}{3c^2 (\omega_r + \omega_0)} - \frac{2(\mu_2/2)^2 (\omega_0 - \omega_r)^4}{3c^2 (\omega_0 - \omega_r)} \right] = - \frac{4\mu_2^2 \omega_0^2}{c^3} \omega_r. \quad (\text{B11})$$

The same result for the torque is obtained for rotation around \mathbf{a}_3 , but rotation of this oscillator around \mathbf{a}_2 would not result in a torque.

Extending this to three incoherent oscillators:

$$\boldsymbol{\mu} = \mu_2 \mathbf{a}_2 \cos \omega_{02} t + \mu_3 \mathbf{a}_3 \cos \omega_{03} t + \mu_1 \mathbf{a}_1 \cos \omega_{01} t \quad (\text{B12})$$

we find

$$\frac{d}{dt} J_i = - \left[\frac{\mu_j^2 \omega_0^2}{c^3} + \frac{\mu_k^2 \omega_0^2}{c^3} \right] \omega_i, \quad (\text{B13})$$

where i, j and k run from 1 to 3 so that if $i = 2$ then $j = 3$ and $k = 1$ and so on; and replace $\omega_{01} \approx \omega_{02} \approx \omega_{03}$ by ω_0 .

If we now consider a grain with symmetry axis \mathbf{a}_1 and $\mu_2 = \mu_3$. The power radiated by in-plane and out-of-plane vibrations is

$$\dot{E}_{ip} = \dot{N}_{ip} \hbar \omega_0 = (\mu_2^2 + \mu_3^2) \frac{\omega_0^4}{3c^3}, \quad \dot{E}_{oop} = \dot{N}_{oop} \hbar \omega_0 = \mu_1^2 \frac{\omega_0^4}{3c^3}, \quad (\text{B14})$$

where \dot{N}_{ip} and \dot{N}_{oop} are the rates of photon emission by in-plane and out-of-plane vibrations. Then

$$\frac{d}{dt} J_{\parallel} = - \left(\frac{3\hbar}{2\pi c I_{\parallel}} \right) (\dot{N}_{ip} \lambda) J_{\parallel}, \quad (\text{B15})$$

$$\frac{d}{dt} J_{\perp} = - \left(\frac{3\hbar}{2\pi c I_{\perp}} \right) \left(\frac{1}{2} \dot{N}_{ip} \lambda + \dot{N}_{oop} \lambda \right) J_{\perp}. \quad (\text{B16})$$

where $J_{\perp} = J_2$, $\lambda = 2\pi c/\omega_0$ is the emitted wavelength.

B3. Electric Dipole Damping

The spinning grain will radiate power, which results in rotational damping of grain. The associated rotational damping time depends on ω .

In the grain body system, the dipole is given by

$$\boldsymbol{\mu} = \mu_1 \mathbf{a}_1 + \mu_2 \mathbf{a}_2 + \mu_3 \mathbf{a}_3. \quad (\text{B17})$$

For simplicity, we assume that $\mu_1^2 \approx \mu_2^2 \approx \mu_3^2 = \frac{1}{3}\mu^2$. The angular velocity $\boldsymbol{\omega}$ in general is not aligned with \mathbf{a}_1 . Thus, the rotation of the grain consists of the rotation about \mathbf{a}_1 with ω_{\parallel} and the rotation with ω_{\perp} about axes perpendicular to \mathbf{a}_1 . The former rotation of the dipole results in the damping for ω_{\parallel} , and the later results in the damping for ω_{\perp} .

Consider first the rotation with angular velocity ω_{\parallel} about \mathbf{a}_1 . After a time t , the dipole moment becomes

$$\begin{aligned} \boldsymbol{\mu} &= \mu_2(\cos \omega_{\parallel} t \mathbf{a}_2 + \sin \omega_{\parallel} t \mathbf{a}_3) + \mu_3(-\sin \omega_{\parallel} t \mathbf{a}_2 + \cos \omega_{\parallel} t \mathbf{a}_3), \\ &= \mu_2 \sqrt{2} \left[-\mathbf{a}_2 \sin \left(\frac{\pi}{4} + \omega_{\parallel} t \right) + \mathbf{a}_3 \cos \left(\frac{\pi}{4} + \omega_{\parallel} t \right) \right], \end{aligned} \quad (\text{B18})$$

The increase of angular momentum of the grain resulting from the rotation is then

$$\frac{d\mathbf{J}}{dt} = -\frac{2}{3c^3} [\dot{\boldsymbol{\mu}} \times \ddot{\boldsymbol{\mu}}] = -\frac{4\mu^2}{9c^3} \omega_{\parallel}^3 \mathbf{a}_1, \quad (\text{B19})$$

where we assumed $\mu_2^2 = \frac{1}{3}\mu^2$. Hence,

$$I_{\parallel} \frac{d\omega_{\parallel}}{dt} = -\frac{4\mu^2}{9c^3} \omega_{\parallel}^3. \quad (\text{B20})$$

Similarly, for the rotation with ω_{\perp} about \mathbf{a}_2 and \mathbf{a}_3 axes, we get

$$I_{\perp} \frac{d\omega_{\perp}}{dt} = -\frac{4\mu^2}{9c^3} \omega_{\perp}^3. \quad (\text{B21})$$

Since $\boldsymbol{\omega}$ is not parallel to \mathbf{a}_1 , let us define characteristic damping times associated with ω_{\parallel} and ω_{\perp} , corresponding to the rotation along and perpendicular to \mathbf{a}_1 .

As in DL98, we can define the damping times due to electric dipole emissions as

$$\left(\frac{1}{\omega_{\parallel,\perp}} \frac{d\omega_{\parallel,\perp}}{dt} \right)_{\text{ed}} = -\frac{I_{\parallel,\perp} \omega_{\parallel,\perp}^2}{3k_{\text{B}} T_{\text{gas}}} \frac{1}{\tau_{\text{ed},\parallel,\perp}}. \quad (\text{B22})$$

Then, combining equations (B20), (B21) and (B22), we obtain

$$\tau_{\text{ed},\parallel} \equiv \frac{3I_{\parallel}^2 c^3}{4\mu^2 k_{\text{B}} T_{\text{gas}}} = 1.6 \times 10^{11} \hat{\rho}^2 a_{-7}^8 \times \frac{(R/L)^{4/3}}{[(a_x/a)^2 \langle Z^2 \rangle + 3.8(\beta/0.4 \text{ D})^2 a_{-7}] T_2} \text{ s}, \quad (\text{B23})$$

and

$$\tau_{\text{ed},\perp} \equiv \frac{3I_{\perp}^2 c^3}{4\mu^2 k_{\text{B}} T_{\text{gas}}} = 4.0 \times 10^{10} \hat{\rho}^2 a_{-7}^8 \times \frac{(R/L)^{4/3} \left(1 + \frac{1}{3}(L/R)^2\right)^2}{[(a_x/a)^2 \langle Z^2 \rangle + 3.8(\beta/0.4 \text{ D})^2 a_{-7}] T_2} \text{ s}, \quad (\text{B24})$$

where μ^2 from DL98b (eq. 20) has been used and $\langle Z^2 \rangle$ is the mean square grain charge.

Using the distribution charge function $f(Z)$ and mean charge $\langle Z \rangle$ obtained by solving equation of ionization equations (see DL98b), we compute damping coefficients $F_n, F_i, F_p, F_{\text{IR}}$ and τ_{ed} . Our new results for F_p, F_{IR} and τ_{ed} are presented in Figures 1, 5 and 6, respectively. For comparison, in Figures 20 we present results from the DL98 model for the WIM and RN.

C. ROTATIONAL EXCITATION

An initially stationary grain will have its rotational kinetic energy increasing at an average rate

$$\frac{d}{dt} \left(\frac{1}{2} I_{\parallel,\perp} \omega_{\parallel,\perp}^2 \right) = \frac{k_{\text{B}} T_{\text{gas}}}{\tau_{\text{H},\parallel,\perp}} \times (G_{n,\parallel,\perp} + G_{i,\parallel,\perp} + G_{p,\parallel,\perp} + G_{\text{IR},\parallel,\perp}), \quad (\text{C1})$$

where the normalized excitation rate G_n is due to impacting neutrals, G_i is due to impacting ions, G_p is due to plasma drag, and G_{IR} is due to recoil from infrared emission, and \parallel, \perp denote excitation along and perpendicular to the grain symmetry axis.

C1. Recoil from Thermal Collisions and Evaporation

For collisional excitations, similar to collisional drag, we have $G_{n,\parallel} = G_{n,\perp}$ and $G_{i,\parallel} = G_{i,\perp}$.

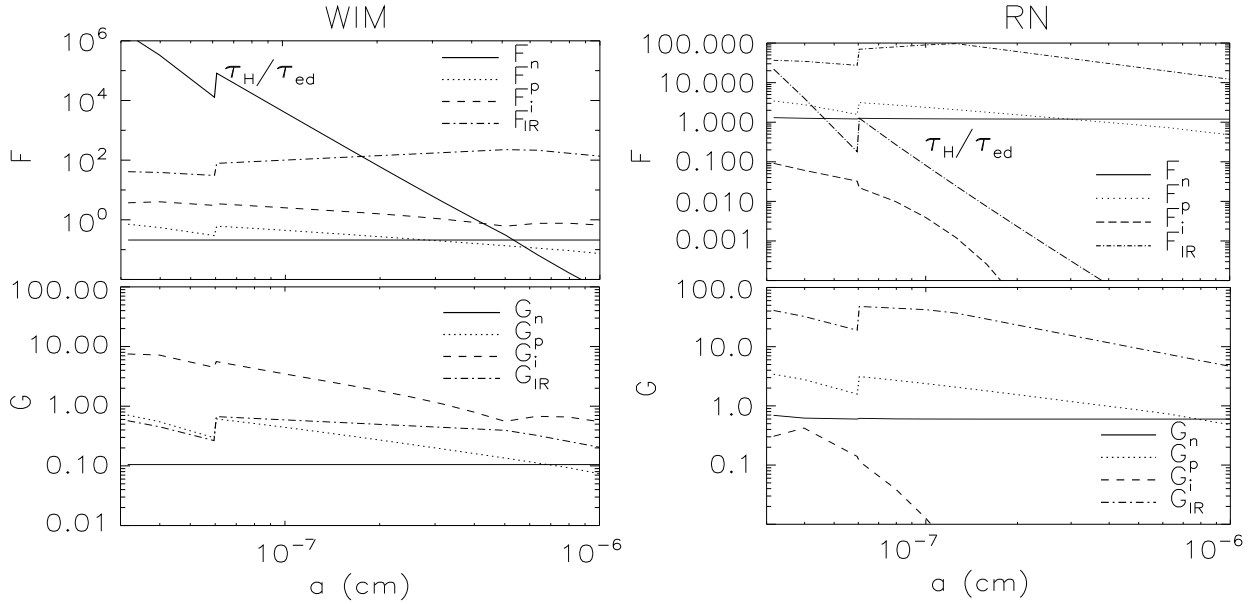


FIG. 20.— *Left*: Damping coefficients F_n, F_i, F_p, F_{IR} and τ_{ed}/τ_H and excitation coefficients G_n, G_i, G_p and G_{IR} from DL98b model as functions of grain size a for WIM. *Right*: Similar to Figure 20 but for the RN.

C2. Excitation by the Plasma

Consider a disk-like grain with dipole moment $\boldsymbol{\mu}$, assumed to be parallel to \mathbf{a}_2 :

$$\boldsymbol{\mu} = |\mu|\mathbf{a}_2. \quad (\text{C2})$$

Let us define the inertial coordinate system $\hat{\mathbf{x}}, \hat{\mathbf{y}}, \hat{\mathbf{z}}$. Grain is assumed to be rotating with angular velocity ω_{\parallel} and ω_{\perp} parallel and perpendicular to the symmetry axis. Initially, $\mathbf{a}_2 \parallel \hat{\mathbf{x}}$, $\mathbf{a}_3 \parallel \hat{\mathbf{y}}$ and $\mathbf{a}_1 \parallel \hat{\mathbf{z}}$. At the time t , the orientation of the grain in the lab system can be determined by two Euler angles θ and ϕ where θ and ϕ are the rotation angles of the grain about \mathbf{a}_1 and \mathbf{a}_3 , respectively.¹² They are given by

$$\mathbf{a}_1 = \cos \theta \hat{\mathbf{z}} + \sin \theta \cos \phi \hat{\mathbf{x}} + \sin \theta \sin \phi \hat{\mathbf{y}}, \quad (\text{C3})$$

$$\mathbf{a}_2 = -\sin \theta \hat{\mathbf{z}} + \cos \theta \cos \phi \hat{\mathbf{x}} + \cos \theta \sin \phi \hat{\mathbf{y}}, \quad (\text{C4})$$

$$\mathbf{a}_3 = \cos \phi \hat{\mathbf{y}} - \sin \phi \hat{\mathbf{x}}. \quad (\text{C5})$$

The trajectory plane of the incoming ion of charge $Z_i e$ with e being the electron charge is $\hat{\mathbf{y}}\hat{\mathbf{z}}$ where $\hat{\mathbf{z}}$ is parallel to the initial direction of ion. The electric field produced by the ion at the grain position is

$$\mathbf{E} = \frac{Z_i e}{r^2} \mathbf{r} = \frac{Z_i e}{r^2} (\cos \alpha \hat{\mathbf{y}} + \sin \alpha \hat{\mathbf{z}}). \quad (\text{C6})$$

The torque induced by the dipole-electric field interaction is given by

$$\begin{aligned} \frac{d\mathbf{J}}{dt} = [\boldsymbol{\mu} \times \mathbf{E}] = |\mu||E| & (\hat{\mathbf{x}}[\sin \theta \cos \alpha + \cos \theta \sin \phi \sin \alpha]) \\ & + |\mu||E| (-\cos \theta \cos \phi \sin \alpha \hat{\mathbf{y}} + \cos \theta \cos \phi \sin \alpha \hat{\mathbf{z}}), \end{aligned} \quad (\text{C7})$$

where equation (B17) has been used. By projecting (C7) onto two rotational axes \mathbf{a}_1 and \mathbf{a}_3 , we obtain

$$\frac{d\omega_{\parallel}}{d\alpha} = \frac{-Z_i e |\mu|}{I_{\parallel} b v} \cos \phi \cos \alpha, \quad \frac{d\omega_{\perp}}{d\alpha} = \frac{-Z_i e |\mu|}{I_{\perp} b v} (\cos \theta \sin \alpha + \sin \theta \sin \phi \cos \alpha), \quad (\text{C8})$$

where $bv = r^2 d\alpha/dt$ has been taken.

The mean rotational excitation due to one ion is then given by

$$\langle (\delta\omega_{\parallel})^2 \rangle = \left(\frac{2Z_i e |\mu|}{I_{\parallel} b v} \right)^2 \mathcal{I}_{\parallel}, \quad \langle (\delta\omega_{\perp})^2 \rangle = \left(\frac{2Z_i e |\mu|}{I_{\perp} b v} \right)^2 \mathcal{I}_{\perp}, \quad (\text{C9})$$

where the factor of 2 comes from the fact that α in the range from 0 to $\pi/2$, instead from $-\pi/2$ to $\pi/2$, or time t from

¹² Ali-Haïmoud et al. (2009) assumes that initial grain orientation is described by θ_0, ϕ_0 , and later, they average over random

θ_0, ϕ_0 . Our assumption is special with $\theta_0 = \phi_0 = 0$, but without losing physical effects

0 to ∞ , and

$$\mathcal{I}_{\parallel} = \left(\int d\alpha \cos \phi \cos \alpha \right)^2, \quad \mathcal{I}_{\perp} = \left(\int d\alpha (\cos \theta \sin \alpha + \sin \theta \sin \phi) \right)^2, \quad (\text{C10})$$

For a neutral grain and the trajectory of ion is straight line, the polar angle α and t are related to each other as follows:

$$\sin \alpha = \frac{vt}{\sqrt{b^2 + v^2 t^2}}, \quad \cos \alpha = \frac{b}{\sqrt{b^2 + v^2 t^2}}, \quad d\alpha = \frac{1}{[1 + (vt/b)^2]} \frac{v dt}{b}, \quad (\text{C11})$$

where we assume that $t = 0$ corresponding to the time when the ion is closest to the grain, i.e., $r = b$. We have, at the time $t=0$, the direction of the grain is random, then at t , we have $\phi = \phi_0 + \omega_{\parallel} t, \theta = \theta_0 + \omega_{\perp} t$ with ϕ_0, θ_0 are random variables.

Therefore, \mathcal{I}_{\parallel} and \mathcal{I}_{\perp} become

$$\mathcal{I}_{\parallel}(x) = \left(\int \cos \phi \cos \alpha d\alpha \right)^2 = \left(\int \cos \omega_{\parallel} t \cos \alpha d\alpha \right)^2 = \left(\int_0^{\infty} d\tau \frac{\cos(x\tau)}{(1 + \tau^2)^{3/2}} \right)^2 = x^2 K_1(x)^2, \quad (\text{C12})$$

$$\begin{aligned} \mathcal{I}_{\perp}(y, y_{\pm}) &= \left(\int [\cos \omega_{\perp} t \sin \alpha + \sin \omega_{\perp} t \sin \omega_{\parallel} t \cos \alpha] d\alpha \right)^2, \\ &= \left(\int_0^{\infty} \frac{\tau \cos(y\tau) d\tau}{(1 + \tau^2)^{3/2}} + \frac{1}{2} (y_+ K_1(y_+) - y_- K_1(y_-)) \right)^2 = \left(H(y) + \frac{1}{2} [y_+ K_1(y_+) - y_- K_1(y_-)] \right)^2, \end{aligned} \quad (\text{C13})$$

where $x = \omega_{\parallel} b/v, y = \omega_{\perp} b/v$ and $y_{\pm} = (\omega_{\parallel} \pm \omega_{\perp}) b/v$. $K_n(x)$ is the modified Bessel function of the second kind, and $H(y)$ is given by

$$H(y) = \int_0^{\infty} \frac{\tau \cos(y\tau) d\tau}{(1 + \tau^2)^{3/2}}. \quad (\text{C14})$$

To calculate (C14) numerically, we note that when the grain rotates much faster than the ion motion, i.e., $y = \omega_{\perp} b/v \gg 1$, the torque gets averaged out. And a truncation of (C14) is $y = 1.3$ is adopted without introducing large uncertainty.

The total excitation rate from all ions with density n_i following normal distribution of velocity is given by

$$\frac{d\langle \delta\omega_{\parallel}^2 \rangle}{dt} = \int_0^{\infty} dv \left(4\pi v^2 n_i v \left(\frac{m_i}{2\pi k_B T_{\text{gas}}} \right)^{3/2} e^{-m_i v^2 / 2k_B T_{\text{gas}}} \right) \int_{b_{\text{max}}}^{\infty} db 2\pi b \left(\frac{Z_i e |\mu|}{I_{\parallel} b v} \right)^2 \mathcal{I}_{\parallel}(x), \quad (\text{C15})$$

$$\frac{d\langle \delta\omega_{\perp}^2 \rangle}{dt} = \int_0^{\infty} dv \left(4\pi v^2 n_i v \left(\frac{m_i}{2\pi k_B T_{\text{gas}}} \right)^{3/2} e^{-m_i v^2 / 2k_B T_{\text{gas}}} \right) \int_{b_{\text{max}}}^{\infty} db 2\pi b \left(\frac{Z_i e |\mu|}{I_{\perp} b v} \right)^2 \mathcal{I}_{\perp}(y, y_{\pm}), \quad (\text{C16})$$

In equations (C15) and (C16), the value b_{max} for a neutral grain is given by

$$b_{\text{max}} = a_{\text{cx}} \sqrt{1 + \frac{\Phi}{u}}, \quad \Phi = \frac{2Z_i^2 e^2}{a_{\text{cx}} k_B T_{\text{gas}}}, \quad u = \frac{v}{v_T} \text{ with } v_T = (2k_B T_{\text{gas}} / m_i)^{1/2}, \quad (\text{C17})$$

and for a charged grain, b_{max} takes the form (see Spitzer 1941)

$$b_{\text{max}} = \begin{cases} 0 & \text{for } \frac{m_i v^2}{2} < \frac{Z_g Z_i e^2}{a_{\text{cx}}} \\ a_{\text{cx}} \left(1 - \frac{2Z_g Z_i e^2}{m_i a_{\text{cx}} v^2} \right)^{1/2} & \text{for } \frac{m_i v^2}{2} > \frac{Z_g Z_i e^2}{a_{\text{cx}}}, \end{cases} \quad (\text{C18})$$

and the upper limit of the integration over the impact factor is constrained by the Debye length $\lambda_D = (k_B T_{\text{gas}} / (4\pi n_e e^2))^{1/2}$.

The dimensionless excitation coefficients for grain-plasma interactions are then

$$G_{\text{p},\parallel} = \frac{d\langle \delta\omega_{\parallel}^2 \rangle}{dt} \frac{I_{\parallel} \tau_{H,\parallel}}{2k_B T_{\text{gas}}}, \quad G_{\text{p},\perp} = \frac{d\langle \delta\omega_{\perp}^2 \rangle}{dt} \frac{I_{\perp} \tau_{H,\perp}}{2k_B T_{\text{gas}}}. \quad (\text{C19})$$

Plugging (C15) and (C16) into the above equations, we obtain

$$G_{\text{p},\parallel,\perp} = \frac{n_i}{n_H} \left(\frac{m_i}{m_H} \right)^{1/2} \left(\frac{Z_i e \mu}{k_B T_{\text{gas}} a_{\text{cx}}} \right)^2 \left(\frac{3}{2} \right) \int_0^{\infty} u e^{-u^2} du \times g_{\parallel,\perp} \quad (\text{C20})$$

where

$$g_{\parallel,\perp} = \int_{b_{\max}/a_{\text{cx}}}^{\infty} \frac{dl}{l} \mathcal{I}_{\parallel,\perp} \left(u \frac{\Omega_{\parallel,\perp}}{l} \right), \text{ and } \Omega_{\parallel,\perp} = \sqrt{\frac{a_{\text{cx}}^2 m_i}{2k_{\text{B}} T_{\text{gas}}}} \omega_{\parallel,\perp}. \quad (\text{C21})$$

Using the Fluctuation-Dissipation theorem, we obtain $F_{\text{p},\parallel} = G_{\text{p},\parallel}$, and $F_{\text{p},\perp} = G_{\text{p},\perp}$. In Figure 1 we show our new results for $G_{\text{p},\parallel}$ and $G_{\text{p},\perp}$ as functions of grain size for neutral grains in the CNM.

Excitation coefficients from DL98b $G_{\text{n}}, G_{\text{i}}, G_{\text{p}}$ and G_{IR} are also shown in the lower panels of Figure 20 for the WIM and RN, respectively.

C3. Rotational Excitation by IR Photons

Consider the case of a grain with dynamical symmetry, with principal values of the moment of inertia tensor $I_1 > I_2 = I_3$, where I_1 is the moment of inertia for rotations around the \mathbf{a}_1 axis. We assume the emission to come from optically active vibrations that are either ‘‘in-plane’’ or ‘‘out-of-plane’’, and we assume the ‘‘in plane’’ oscillators to be symmetrically distributed around the \mathbf{a}_1 -axis (i.e., equal numbers oscillating in the \mathbf{a}_2 - and \mathbf{a}_3 -directions).

Let P_2, P_3 , and P_1 be the power radiated by vibrational modes with electric dipole moment oscillating in the \mathbf{a}_2 -, \mathbf{a}_3 -, and \mathbf{a}_1 -directions. For electric dipole radiation, we can imagine that each oscillator radiates 50% of its power in each of the two cardinal directions orthogonal to the dipole.

For a nonrotating (or slowly rotating) grain, the angular momentum will undergo a random walk with

$$\left\langle \frac{d}{dt} J_i^2 \right\rangle = \frac{1}{2} \frac{(P_j + P_k)}{h\nu} 2\hbar^2, \quad (\text{C22})$$

where i, j, k run from 1 to 3 and the vector basis $\mathbf{a}_i \mathbf{a}_j \mathbf{a}_k$ follow right-handed rule.

Thus, defining $J_{\perp}^2 \equiv J_2^2 = J_3^2$, and noting that P_2 and P_3 are in-plane vibrations, and P_1 is out-of-plane:

$$\left\langle \frac{d}{dt} J_{\perp}^2 \right\rangle = \frac{1}{2} \left[\frac{1}{2} \dot{N}_{ip} + \dot{N}_{oop} \right] 2\hbar^2, \quad \left\langle \frac{d}{dt} J_{\parallel}^2 \right\rangle = \frac{1}{2} \dot{N}_{ip} 2\hbar^2 \quad (\text{C23})$$

D. COLLISION OF IONS WITH GRAINS

The damping and excitation coefficients for the collision of ions with grain were calculated in DL98b, and refined in Ali-Haïmoud et al. (2009). The later study showed that the calculations by DL98b where the effects of dipole were disregarded remain valid. Thus, below we also disregard the effect of dipole in calculating the collision rate for ion-grain collision. The collision rate of ions with density n_i with a grain of size a is

$$R_i = n_i \int_0^{\infty} v \pi b_{\max}^2 4\pi v^2 f(v) dv = n_i \int_0^{\infty} v \pi b_{\max}^2 4\pi v^2 A \exp\left(\frac{-m_i v^2}{2k_{\text{B}} T_{\text{gas}}}\right) dv, \quad (\text{D1})$$

where $A = (2k_{\text{B}} T_{\text{gas}}/m_i \pi)^{-3/2}$, and b_{\max} is the critical impact factor so that all incoming ions with impact factor $b \leq b_{\max}$ collide with the grain.

D1. Neutral grain

For neutral grain, b_{\max} is given by equation (C17), thus, plugging (C17) into (D1) and performing the integral, we obtain

$$R_i(Z_{\text{g}} = 0) = n_i \pi a^2 \left(\frac{8k_{\text{B}} T_{\text{gas}}}{m_i \pi} \right)^{1/2} \left[1 + \frac{\sqrt{\pi}}{2} \left(\frac{2Z_i^2 e^2}{ak_{\text{B}} T_{\text{gas}}} \right)^{1/2} \right]. \quad (\text{D2})$$

The rms angular momentum per collision is obtained by dividing the rms angular momentum to the collision rate. For the ion-neutral collision, we have

$$\langle \delta J^2 \rangle = m_i k_{\text{B}} T_{\text{gas}} a^2 \frac{2 + 3\sqrt{\pi/2\tau} + 2/\tau}{1 + \sqrt{\pi/2\tau}}, \quad \text{with } \tau = \frac{ak_{\text{B}} T_{\text{gas}}}{e^2} = 60 \left(\frac{a}{10^{-7} \text{ cm}} \right) \left(\frac{T_{\text{gas}}}{10^4 \text{ K}} \right). \quad (\text{D3})$$

D2. Charge grain

For a charge grain, using the critical impact factor from (C18) for (D1) we obtain

$$R_i(Z_{\text{g}} \neq 0) = n_i \pi a^2 \left(\frac{8k_{\text{B}} T_{\text{gas}}}{m_i \pi} \right)^{1/2} g \left(\frac{Z_{\text{g}} Z_i e^2}{ak_{\text{B}} T_{\text{gas}}} \right), \quad (\text{D4})$$

where $g(x) = 1 - x$ for $x < 0$ and $g(x) = e^{-x}$ for $x > 0$

The collision of one ion with the negatively-charged grain has rms angular momentum per collision for this case given by

$$\langle \delta J^2 \rangle = m_i k_{\text{B}} T_{\text{gas}} a^2 \frac{2 - 2\phi + \phi^2}{1 - \phi}, \quad \text{with } \phi = \frac{Z_{\text{g}} e^2}{ak_{\text{B}} T_{\text{gas}}}. \quad (\text{D5})$$

Taking into account the grain charge distribution, the final form for collision rate becomes

$$R_i = f(Z_g = 0)n_i\pi a^2 \left(\frac{8k_B T_{\text{gas}}}{m_i \pi} \right)^{1/2} \left[1 + \frac{\sqrt{\pi}}{2} \left(\frac{2Z_i^2 e^2}{ak_B T_{\text{gas}}} \right)^{1/2} \right] + \sum_{Z_g \neq 0} f(Z_g)n_i\pi a^2 \left(\frac{8k_B T_{\text{gas}}}{m_i \pi} \right)^{1/2} g \left(\frac{Z_g Z_i e^2}{ak_B T_{\text{gas}}} \right), \quad (\text{D6})$$

where $f(Z_g)$ is the grain charge distribution function.

E. TRANSFORMATION OF COORDINATE SYSTEMS

Damping coefficient $A_i = \langle \Delta J_i / \Delta t \rangle$ and diffusion coefficients $B_{ij} = \langle \Delta J_i \Delta J_j / \Delta t \rangle$ are usually derived in the body coordinate system, while we are interested in the evolution of grain angular momentum in the inertial coordinate system. Let us define an inertial coordinate system $\mathbf{e}_1 \mathbf{e}_2 \mathbf{e}_3$ in which the direction \mathbf{J} is described by the angle ξ between \mathbf{J} with \mathbf{e}_1 , and the azimuthal angle χ (see Figure 2 in Roberge & Lazarian 1999 in which angles ϕ , β are replaced by χ , ξ). To obtain these coefficients in the lab coordinate system, we first transform the body system \mathbf{a}_i to the external system $\hat{\mathbf{x}}\hat{\mathbf{y}}\hat{\mathbf{z}}$ where $\hat{\mathbf{z}}\parallel\mathbf{J}$ and $\hat{\mathbf{x}}, \hat{\mathbf{y}} \perp \mathbf{J}$ (see Figure 7). Then, we perform the transformation from $\hat{\mathbf{x}}\hat{\mathbf{y}}\hat{\mathbf{z}}$ system to the inertial system $\mathbf{e}_1 \mathbf{e}_2 \mathbf{e}_3$. In the body system, the damping coefficients are given by

$$A_i^b = \left\langle \frac{\Delta J_i^b}{\Delta t} \right\rangle = -\frac{J_i}{\tau_{\text{gas},i}} - \frac{J_i^3}{\tau_{\text{ed},i}} \left(\frac{1}{3I_i k_B T_{\text{gas}}} \right), \quad (\text{E1})$$

where $t_{\text{gas},i} = F_{\text{tot},i} / \tau_{\text{H},\parallel}$ and $i = x, y$ and z with $z\parallel\mathbf{a}_1$. The diffusion coefficients, $B_{ij}^b = \langle \Delta J_i^b \Delta J_j^b / \Delta t \rangle$ with $B_{ij}^b = 0$ for $i \neq j$ are related to the excitation coefficients as follows:

$$B_{zz}^b = B_{\parallel} = \frac{2I_{\parallel} k_B T_{\text{gas}}}{\tau_{\text{H},\parallel}} G_{\text{tot},\parallel}, \quad \text{and} \quad B_{xx}^b = B_{yy}^b = B_{\perp} = \frac{2I_{\perp} k_B T_{\text{gas}}}{\tau_{\text{H},\perp}} G_{\text{tot},\perp}. \quad (\text{E2})$$

Transforming the vector A_i^b and matrix B_{ij}^b from the body system to the inertial system, and averaging over the fast precession of \mathbf{a}_1 about \mathbf{J} , we obtain damping coefficient (see Lazarian & Roberge 1997)

$$A_i = \left\langle \frac{\Delta J_i}{\Delta t} \right\rangle = -\frac{J_i}{\tau_{\text{gas,eff}}} - \frac{J_i^3}{\tau_{\text{ed,eff}}} \left(\frac{1}{3I_{\parallel} k_B T_{\text{gas}}} \right), \quad \text{for } i = x, y, z, \quad (\text{E3})$$

where the effective gas damping reads

$$\tau_{\text{gas,eff}} = \tau_{\text{H},\parallel} F_{\text{tot},\parallel} \frac{1}{\cos^2 \theta + \gamma_{\text{H}} \sin^2 \theta}, \quad (\text{E4})$$

and the effective time for electric dipole damping is given by

$$\tau_{\text{ed,eff}} = \tau_{\text{ed},\parallel} \frac{1}{\cos^4 \theta + \gamma_{\text{ed}} \sin^4 \theta}. \quad (\text{E5})$$

where θ is the angle between \mathbf{a}_1 and \mathbf{J} , and

$$\gamma_{\text{H}} = \frac{F_{\text{tot},\perp} \tau_{\text{H},\parallel}}{F_{\text{tot},\parallel} \tau_{\text{H},\perp}}, \quad \gamma_{\text{ed}} = \frac{I_{\parallel} \tau_{\text{ed},\parallel}}{I_{\perp} \tau_{\text{ed},\perp}} = h^3. \quad (\text{E6})$$

If the coupling of parallel and perpendicular rotation is accounted for, then the electric dipole damping is increased by a small amount, and equation (E5) is rewritten as (communication with C Hirata)

$$\tau_{\text{ed,eff}} = \tau_{\text{ed},\parallel} \frac{1}{\cos^4 \theta + \gamma_{\text{ed}} \sin^4 \theta + (h^3 + 3h) \sin^2 \theta \cos^2 \theta / 2}. \quad (\text{E7})$$

We can see that for disk-like grains, $\gamma_{\text{H}} > 1$, and $\tau_{\text{gas,eff}} < \tau_{\text{H},\parallel} F_{\text{tot},\parallel}$, which results in faster gas damping time.

The diffusion coefficients in the inertial system \mathbf{e}_i , B_{zz} and B_{xx}, B_{yy} are given by

$$B_{zz} = B_{\parallel} \left(\frac{1}{2} \sin^2 \theta \sin^2 \xi + \cos^2 \theta \cos^2 \xi \right) + B_{\perp} \left(\frac{1}{2} [1 + \cos^2 \theta] \sin^2 \xi + \sin^2 \theta \cos^2 \xi \right), \quad (\text{E8})$$

$$B_{xx} = B_{\parallel} \left(\frac{1}{2} \sin^2 \theta [\cos^2 \chi + \sin^2 \chi \cos^2 \xi] + \cos^2 \theta \sin^2 \chi \sin^2 \xi \right) + B_{\perp} \left(\frac{1}{2} [1 + \cos^2 \theta] [\cos^2 \chi + \sin^2 \chi \cos^2 \xi] + \sin^2 \theta \sin^2 \chi \sin^2 \xi \right), \quad (\text{E9})$$

$$B_{yy} = B_{\parallel} \left(\frac{1}{2} \sin^2 \theta [\sin^2 \chi + \cos^2 \chi \cos^2 \xi] + \cos^2 \theta \sin^2 \chi \sin^2 \xi \right) + B_{\perp} \left(\frac{1}{2} [1 + \cos^2 \theta] [\sin^2 \chi + \cos^2 \chi \cos^2 \xi] + \sin^2 \theta \sin^2 \chi \sin^2 \xi \right), \quad (\text{E10})$$

where ξ is the angle between \mathbf{J} and \mathbf{e}_1 , and χ is the azimuthal angle of \mathbf{J} in the inertial system \mathbf{e}_i .

In the presence of fast internal fluctuations, we need to average the damping and diffusion coefficients over θ . Therefore, the terms containing θ in above equations are replaced by the averaged values, i.e., $\langle \cos^2 \theta \rangle = \int_0^\pi \cos^2 \theta f_{\text{LTE}}(\theta) d\theta$,

$\langle \sin^2 \theta \rangle = \int_0^\pi \sin^2 \theta f_{\text{LTE}}(\theta) d\theta$. Note that we do not average the damping and diffusion coefficients over the precession angle χ here because the effect of magnetic field which results in the fast precession of \mathbf{J} about the magnetic field is disregarded.

Then, the Langevin equations in the inertial system become

$$dJ_i = A_i dt + \sqrt{B_{ii}} dq_i, \text{ where } \langle dq_i^2 \rangle = dt, \text{ and } i = x, y, z. \quad (\text{E11})$$

F. DIPOLE EMISSION OF A TORQUE-FREELY ROTATING GRAIN

Let us consider the simple case where the dipole is given by

$$\boldsymbol{\mu} = \mu_{\parallel} \mathbf{a}_1 + \mu_{\perp} \mathbf{a}_2 \quad (\text{F1})$$

in the body system. In an external coordinate system $\hat{\mathbf{x}}\hat{\mathbf{y}}\hat{\mathbf{z}}$ (see Figure 7), \mathbf{a}_1 , \mathbf{a}_2 and \mathbf{a}_3 are described as

$$\mathbf{a}_1 = \sin \phi \sin \theta \hat{\mathbf{x}} - \cos \phi \sin \theta \hat{\mathbf{y}} + \cos \theta \hat{\mathbf{z}}, \quad (\text{F2})$$

$$\mathbf{a}_2 = (\cos \phi \cos \psi - \sin \phi \sin \psi \cos \theta) \hat{\mathbf{x}} + (\sin \phi \cos \psi + \cos \phi \sin \psi \cos \theta) \hat{\mathbf{y}} + \sin \psi \sin \theta \hat{\mathbf{z}}, \quad (\text{F3})$$

$$\mathbf{a}_3 = -(\cos \phi \sin \psi + \sin \phi \cos \psi \cos \theta) \hat{\mathbf{x}} + (-\sin \phi \sin \psi + \cos \phi \cos \psi \cos \theta) \hat{\mathbf{y}} + \cos \psi \sin \theta \hat{\mathbf{z}}, \quad (\text{F4})$$

where ϕ, ψ and θ are Euler angles (see Figure 7).

Let us now consider the torque-free motion of an axisymmetric grain with the angular momentum \mathbf{J} and the ratio of inertia moments h . For this case, the symmetry axis \mathbf{a}_1 precesses about \mathbf{J} with constant angle θ and the rate $\dot{\phi}$, and the grain rotates about the symmetry axis with the rate $\dot{\psi}$. They are given by (Landau & Lifshitz 1976)

$$\dot{\phi} = \frac{J}{I_{\perp}}, \quad \dot{\psi} = \frac{J}{I_{\parallel}} \cos \theta (1 - h). \quad (\text{F5})$$

Precession and rotation of the grain with respect to \mathbf{J} results in an instantaneous acceleration for dipole moment:

$$\ddot{\boldsymbol{\mu}} = \mu_{\parallel} \ddot{\mathbf{a}}_1 + \mu_{\perp} \ddot{\mathbf{a}}_2, \quad (\text{F6})$$

where $\ddot{\mathbf{a}}_1$ and $\ddot{\mathbf{a}}_2$ are given by

$$\ddot{\mathbf{a}}_1 = -\dot{\phi}^2 \sin \theta (\sin \phi \hat{\mathbf{x}} - \cos \phi \hat{\mathbf{y}}), \quad (\text{F7})$$

$$\begin{aligned} \ddot{\mathbf{a}}_2 = & \left[-\dot{\phi}^2 (\cos \phi \cos \psi - \sin \phi \sin \psi \cos \theta) - 2\dot{\phi}\dot{\psi} (-\sin \phi \sin \psi + \cos \phi \cos \psi \cos \theta) - \dot{\psi}^2 (\cos \phi \cos \psi - \sin \phi \sin \psi \cos \theta) \right] \hat{\mathbf{x}} \\ & + \left[-\dot{\phi}^2 (\sin \phi \cos \psi + \cos \phi \sin \psi \cos \theta) - 2\dot{\phi}\dot{\psi} (\cos \phi \sin \psi + \sin \phi \cos \psi \cos \theta) - \dot{\psi}^2 (\sin \phi \cos \psi + \cos \phi \sin \psi \cos \theta) \right] \hat{\mathbf{y}} \\ & - \dot{\psi}^2 \sin \psi \sin \theta \hat{\mathbf{z}}, \end{aligned} \quad (\text{F8})$$

$$\begin{aligned} \ddot{\mathbf{a}}_3 = & \left[\dot{\phi}^2 (\cos \phi \sin \psi + \sin \phi \cos \psi \cos \theta) + 2\dot{\phi}\dot{\psi} (\sin \phi \cos \psi + \cos \phi \sin \psi \cos \theta) + \dot{\psi}^2 (\cos \phi \sin \psi + \sin \phi \cos \psi \cos \theta) \right] \hat{\mathbf{x}} \\ & + \left[\dot{\phi}^2 (\sin \phi \sin \psi - \cos \phi \cos \psi \cos \theta) - 2\dot{\phi}\dot{\psi} (\cos \phi \cos \psi - \sin \phi \sin \psi \cos \theta) + \dot{\psi}^2 (\sin \phi \sin \psi - \cos \phi \cos \psi \cos \theta) \right] \hat{\mathbf{y}} \\ & - \dot{\psi}^2 \cos \psi \sin \theta \hat{\mathbf{z}}, \end{aligned} \quad (\text{F9})$$

Solving equation (F5) for Euler angles, and plugging into equation (F6) with the usage of equations (F7) and (F9) we obtain the dipole acceleration $\ddot{\boldsymbol{\mu}}$ as functions of time. Performing Fourier transform for the components of $\ddot{\boldsymbol{\mu}}$ gives us the spectrum and frequency of electric dipole emission.

The dipole emission power of this torque-freely rotating grain can be obtained by averaging the $\ddot{\boldsymbol{\mu}}^2$ over Euler angles ϕ and ψ in the range from 0 to 2π :

$$P_{\text{ed}}(J, \theta) = \frac{2}{3c^3} \langle \ddot{\boldsymbol{\mu}}^2 \rangle \equiv \int_0^{2\pi} \int_0^{2\pi} \frac{d\phi}{2\pi} \frac{d\psi}{2\pi} \frac{2}{3c^3} \ddot{\boldsymbol{\mu}}^2 \quad (\text{F10})$$

REFERENCES

- Ali-Haïmoud, Y., Hirata, C. M., Dickinson, C., & Readhead, A. 2009, MNRAS, 395, 1055
Allers, K. N., Jaffe, D. T., Lacy, J. H., Draine, B. T., Richter, M. J. 2009, ApJ, 630, 368
Anderson, N., & Watson, W.D. 1993, A&A, 270, 477
Bennett, C. L. et al. 2003, ApJS, 148, 97
Bouchet, F. R., Prunet, S., & Sethi, Shiv K. 1999, MNRAS, 302, 663
Boughn, S. P., & Pober, J. C. 2007, ApJ, 661, 938
de Oliveira-Costa et al. 1999, ApJ, 527, 9
de Oliveira-Costa et al. 2002, ApJS, 567, 363
Dobler, G., Draine, B., & Finkbeiner, D. P. 2009, ApJ, 699, 1374
Draine, B.T., & Lazarian, A. 1998, ApJ, 494, L19 (DL98a)
Draine, B. T., & Lazarian, A. 1998, ApJ, 508, 157 (DL98b)
Draine, B. T., & Li, A. 2001, ApJ, 551, 807
—. 2007, ApJ, 657, 810 (DL07)
Draine, B.T., & Sutin, B. 1987, ApJ, 320, 803
Efstathiou, G. 2003, MNRAS, 346, 26
Erickson, W.C, 1957, ApJ, 126, 480
Ferrara, A., & Dettmar, R.-J. 1994, ApJ, 427, 155
Finkbeiner, D. P., Langston, G. I., & Minter, A. H. 2004, ApJ, 617, 350
Gardiner, C. W. 1983, Handbook of Stochastic Method (Berlin: Springer)

- Gold, B., Bennett, C. L., Hill, R. S., et al. 2009, ApJS, 180, 265
- Gold, B., Odegard, N., Weiland, J. L., et al. 2010, ApJS, submitted
- Hoang, T., & Lazarian, A. 2008, MNRAS, 388, 117
- Hoang, T., & Lazarian, A. 2009, ApJ, 695, 1457
- Jones, R.V., & Spitzer, L. 1967, ApJ, 147, 943
- Kogut, A. et al. 1996a, ApJ, 460, 1
- Kogut, A. et al. 1996a, ApJL, 464, 5
- Landau L.D, & Lifshitz E. M. 1976, Mechanics (Oxford: Pergamon)
- Lazarian, A. 1994, MNRAS, 268, 713
- Lazarian, A. 1995, MNRAS, 274, 679
- Lazarian, A. 2007, J. Quant. Spectrosc. Rad. Trans., 106, 225
- Lazarian, A., & Draine, B.T. 1999, ApJ, 520, L67
- Lazarian, A., & Hoang, T. 2009, arXiv 0901.0146
- Lazarian, A., & Roberge, W. 1997, ApJ, 484, 230
- Li, A., & Draine, B. T. 2001, ApJ, 554, 778
- Mathis, J.S., Mezger, P.G., & Panagia, N. 1983, A&A, 128, 212
- Purcell, E.M. 1979, ApJ, 231, 404.
- Ragot, B.R. 2002, ApJ, 568, 232 Roberge & Lazarian 1999
- Roberge, W., DeGraf, T.A., Flaherty, J.E. 1993, ApJ, 418, 287
- Silsbee, K., Ali-Haïmoud, Y., & Hirata, C., arXiv 1003.4732v1
- Sironi, L., & Draine, B.T. 2009, ApJ, 698, 1292
- Tegmark et al. 2000, ApJ, 530, 133
- Ysard, N., Verstraete, L. 2009, arXiv: 09063102
- Weingartner, J. 2009, ApJ, 690, 875
- Weingartner, J.C., & Draine, B.T. 2001b, ApJS, 134, 263